

Synthesis and Electrochemical Study of PtIr and PtRu Nanomaterials

A Thesis Presented to

The Faculty of Graduate Studies

Lakehead University

By

WALAA S. ALAMMARI

In partial fulfillment of the requirements for the degree of

Master of Science

April 2015

© Walaa S. Alammari, 2015

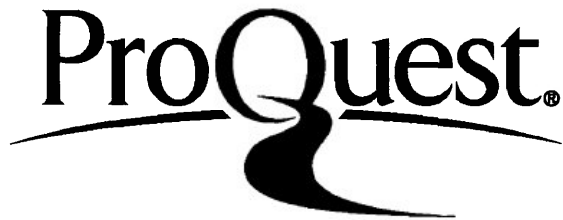
ProQuest Number: 10611967

All rights reserved

INFORMATION TO ALL USERS

The quality of this reproduction is dependent upon the quality of the copy submitted.

In the unlikely event that the author did not send a complete manuscript and there are missing pages, these will be noted. Also, if material had to be removed, a note will indicate the deletion.



ProQuest 10611967

Published by ProQuest LLC (2017). Copyright of the Dissertation is held by the Author.

All rights reserved.

This work is protected against unauthorized copying under Title 17, United States Code
Microform Edition © ProQuest LLC.

ProQuest LLC.
789 East Eisenhower Parkway
P.O. Box 1346
Ann Arbor, MI 48106 - 1346

Abstract

The rapidly growing need for clean energy on a global scale has led to the emergence of new fields of scientific research to facilitate the discovery and development of novel energy sources, such as fuel cells, which generate significantly lower environmentally harmful contaminants, in contrast to traditional fossil fuels. The direct methanol fuel cell (DMFC) is a promising future energy technology alternative due to its high energy conversion efficiency, minimal level of pollutant emissions, the attractive energy density of methanol fuel, and its ease of availability. To date, Platinum (Pt) has been the most effective catalyst in DMFCs, and has been utilized as anodic and cathodic catalysts in many other applications. In this M.Sc. thesis, Platinum-Iridium (PtIr)-and Platinum-Ruthenium (PtRu)-based nanomaterials have been synthesized and investigated to demonstrate their application in DMFCs, as anodic and cathodic catalysts. Analyses of the surfaces of synthesized Pt, and PtIr-and PtRu-based nanomaterials were performed by scanning electron microscopy (SEM), energy dispersive X-ray spectrometry (EDX), X-ray diffraction (XRD), and X-ray photoelectron spectroscopy (XPS). The electrochemical properties of the synthesized nanomaterials were elucidated via cyclic voltammetry (CV), chronoamperometry (CA), and electrochemical impedance spectroscopy (EIS).

A nanostructured TiO₂NT substrate was used for these investigations. The synthesis of Titanium dioxide nanotube materials (TiO₂NT) was accomplished through the anodization of TiO₂NTs possess a highly active surface area following their treatment with UV light. Pt and Ir were subsequently deposited onto the TiO₂NTs, and the resulting TiO₂NT/PtIr electrodes were fabricated by chemical reduction method. Several TiO₂NT/PtIr and TiO₂NT/PtRu electrodes with different compositions were studied and compared with the Pt modified TiO₂NT electrodes. The fabricated Pt and PtIr, and PtRu catalysts were characterized by SEM, EDX, whereas the

electrocatalytic activity toward methanol oxidation was investigated by CV, CA, and EIS. The results indicated that the PtIr/TiO₂NT with a Pt:Ir ratio of 60:40 and PtRu/TiO₂NT with a Pt:Ru composition of 60:40 composites possessed the highest methanol oxidation activity and stability.

In addition, a series of reduced graphene oxide (rGO) and PtRu nanoparticle nanocomposites with different atomic ratios of Pt:Ru (100:0, 84:16, 69:31, 64:36, 42:58 and 0:100) were deposited onto the TiO₂NTs (as TiO₂NT/rGO-PtRu) and tested for their impacts on the oxygen reduction reaction (ORR) in the DMFCs. TiO₂NT/rGO-PtRu nanocomposites were fabricated using a electrochemical deposition technique, and then characterized by SEM, EDX, and XRD. The electrocatalytic activity was subsequently investigated by CV, CA, and EIS. The Pt:Ru with a ratio of 64:36 exhibited the highest stability and electrocatalytic activity toward ORR, which is promising for environmental and green energy applications.

Acknowledgments

I would like to express my utmost gratitude and thanks to my supervisor Dr. Aicheng Chen for his knowledge and advice the course of my M. Sc. degree. This thesis would not have been possible without continued support throughout the research period. He has given me the tools and confidence required for a future in this field. I would also like to extend my greatest appreciation to my thesis committee, Dr. Wely Floriano and Dr. Craig Mackinnon for their guidelines and feedback on my thesis.

An extended thank goes out to the entire Lakehead University Chemistry Department and Graduate Studies. Thank you to Dr. Guosheng Wu and Jiali Wen for their assistance in the Lakehead University Instrumentation Lab. Surface Interface Ontario/Chemical Engineering & Applied Chemistry at the University of Toronto for carrying out the XPS analysis. I would like also to thank Saudi Cultural Bureau in Canada for their support especially King Abdullah scholarship program for their funding. As well as, I would like to thank Saudi Embassy in Ottawa for their help and advice during the time of my study.

All my fellow lab members of Dr.Chen's research group deserve acknowledgement. I especially want to thank Dr. Maduraiveeran Govindhan, Dr. Gousheng Wu, Dr. Sapanbir Thind, Jiali Wen, Xin Chang, Cassandra Ostrom, and Frank Boehm for all their support and encouragement.

Lastly, I would also like to express my deep appreciation to my family especially my father Saleh and my mother Fahmiah for encouraging me. I am indebted to my brother Abdullah for his support during the hard time. I'm thankful to my friends for all the moral support they provide.

Table of contents

Abstract.....	i
Acknowledgements.....	iii
Table of contents.....	iv
List of figures.....	vi
List of tables.....	ix
List of Abbreviations and Symbols.....	x

Chapter 1: Introduction

1.1 Introduction.....	1
1.2 Fuel cell principals	2
1.3 Types of fuel cells	3
1.4 Anodic electrocatalysts for DMFCs.....	11
1.5 Electrocatalyst for oxygen reduction reaction (ORR) in FCs	13
1.6 Scope of this thesis.....	15
References.....	15

Chapter 2: Experimental Methods

2.1 Introduction	22
2.2 Chemicals and materials	22
2.3 Fabrication of nanomaterials.....	22
2.4 Surface analysis	24
2.5 Electrochemical experiments	25
2.6 Summary.....	25
References	26

Chapter 3: Synthesis and Electrochemical Study of Pt-Ir Nanoparticles Deposited on TiO₂NTs for Methanol Oxidation

3.1 Introduction.....	27
3.2 Experimental methods.....	28

3.3	Pt-Ir Surface analysis and composition.....	29
3.4	The electrochemical behaviours of the TiO ₂ NT/PtIr nanostructures.....	30
3.5	Conclusions.....	40
	References.....	41
Chapter 4: Synthesis and electrochemical study of Pt-Ru nanoparticles deposited on TiO ₂ NTs for methanol oxidation		
4.1	Introduction.....	44
4.2	Experimental and methods.....	45
4.3	Pt-Ru surface analysis and composition.....	46
4.4	Electrochemical behavior of the TiO ₂ NT/PtRu nanostructures.....	49
4.5	Electrooxidation of methanol oxidation on the TiO ₂ NT/Pt and TiO ₂ NT/PtRu nanostructures	49
4.6	Conclusions.....	55
	References.....	55
Chapter 5: Modification of TiO ₂ nanotubes with PtRu/Graphene nanocomposites for enhanced oxygen reduction reaction		
5.1	Introduction.....	58
5.2	Experimental and methods	60
5.3	Surface morphology and compositions of Pt-Ru catalysts.....	62
5.4	Electrochemistry behavior of the TiO ₂ NT/rGO-PtRu nanostructures.....	67
5.5	Conclusions.....	76
	References.....	77
Chapter 6: Summary and future work		
6.1	PtIr nanoparticles deposited on TiO ₂ NTs for DMFC.....	80
6.2	PtRu nanoparticles deposited on TiO ₂ NTs for DMFC.....	81
6.3	Oxygen reduction reaction on the TiO ₂ NT/rGO-PtRu electrodes.....	81
6.4	Closing remarks and future work.....	82

List of Figures:

Figure 3.1 SEM images of: (A) the formed TiO₂NTs; and (B) the TiO₂NT/PtIr electrode with the Pt:Ir ratio of 60:40.

Figure 3.2 (A) EDX Spectrum of the TiO₂NT/PtIr electrode with the Pt:Ir ratio of 60:40. (B) EDX elemental mapping of Pt; and (C) EDX elemental mapping of Ir of the same TiO₂NT/PtIr electrode.

Figure 3.3 (a) Cyclic voltammograms of the effect of different loadings of PtIr on TiO₂ in 0.5M H₂SO₄, under a scan rate of 20 mV/s in different potential ranges; short (a) and long (b), the CVs methanol oxidation of different PtIr loads on TiO₂ in 0.5M of H₂SO₄ +0.1M CH₃OH under a scan rate of 20 mV/s(c) .

Figure 3.4 (a) Cyclic voltammograms of the effect of different PtIr compositions on TiO₂ in 0.5M H₂SO₄, under a scan rate of 20 mV/s in different potential ranges; short (a) and long (b), the CVs of methanol oxidation of different PtIr compositions on TiO₂ in 0.5M of H₂SO₄ +0.1M CH₃OH, under a scan rate of 20 mV/s(c)

Figure 3.5 Chronoamperometric curves of CH₃OH electrooxidation on TiO₂/PtIr catalysts in 0.1 M CH₃OH + 0.5 M H₂SO₄ at a potential of 350mV, and 650mV vs SCE shown in parts (A) and (B) in 0.1 M CH₃OH + 0.5 M H₂SO₄.

Figure 3.6 Nyquist plots of the TiO₂NT/Pt, and TiO₂NT/PtIr electrodes with Pt:Ir 70:30, 60:40 compositions in the nanocomposites on the TiO₂NT electrodes recorded in 0.5M H₂SO₄ + 0.1 M

Figure 4.1 SEM images of the TiO₂NTs (A), the TiO₂NT electrode under high magnification (B), TiO₂NT/PtRu nanoparticles under low-magnification (C), the PtRu nanoparticles on the TiO₂NT (D).

Figure 4.2 (A) EDS of the TiO₂NT/PtRu electrodes with the TiO₂NT/ PtRu (60:40) ratio, Elemental mapping of the Ti (B), Pt (C) and Ru (D) obtained at the Pt-Ru (60:40) electrode.

Figure 4.3 Cyclic voltammograms of the effects of different compositions of Pt-Ru on TiO₂NTs in 0.5M H₂SO₄ at a scan rate of 20 mV/s and potential of -0.225V to 1.200V

Figure 4.4 (a) The CVs of methanol oxidation at PtRu/ TiO₂NTs and CVs with Ar TiO₂NTs/ PtRu in 0.5M of H₂SO₄ +0.1M CH₃OH under a scan rate of 20 mV/s. (b) CVs of methanol oxidation of different Pt-Ru ratio on TiO₂ NTs in 0.5M of H₂SO₄ +0.1M CH₃OH at a scan rate of 20mVs-1.

Figure 4.5 CVs of CO oxidation of different Pt-Ru compositions on TiO₂ NTs in 0.5M H₂SO₄ at a scan rate of 20 mV/s.

Figure 4.6 Chronoamperometric curves of CH₃OH electrooxidation on the TiO₂NT/PtRu catalysts in 0.1 M CH₃OH + 0.5 M H₂SO₄ at a potential of both 0. 60 V and 0.65 V.

Figure 5.1 SEM images of the TiO₂NTs (A) and TiO₂NT/rGO-PtRu (64:36) electrode (B).

Figure 5.2 (A) EDS of the TiO₂NT/rGO-PtRu electrodes with their composition of Pt:Ru 84:16 (a), 69:31 (b), 64:36 (c) and 42:58 (d) in the nanocomposites on the TiO₂NT (Peaks marked with asterisks are derived from Ti). Elemental mapping of the Pt (B), Ru (C) and C (D) obtained at the TiO₂NT/rGO-PtRu (64:36) electrode.

Figure 5.3 XRD of the TiO₂NT/rGO-PtRu electrodes with their composition of Pt:Ru 84:16 (a), 69:31 (b), 64:36 (c) and 42:58 (d) in the nanocomposites on the TiO₂NT (Peaks marked with asterisks are derived from the anatase phase of TiO₂).

Figure 5.4 XPS spectra of the C 1s and Ru 3d regions (A), Pt 4f region (B) and Ti 2p region (C) for the TiO₂NT/rGO-PtRu nanocomposite.

Figure 5.5 CVs of the TiO₂NT (magenta), TiO₂NT/rGO (blue), TiO₂NT/rGO-Pt (red), TiO₂NT/rGO-Ru (black), TiO₂NT/PtRu (cyan) and TiO₂NT/rGO-PtRu (60:40) (green) electrodes recorded in O₂-saturated 0.1 M KOH, scan rate of 20 mV/s.

Figure 5.6 CVs of the TiO₂NT/rGO-PtRu electrodes with their composition of Pt:Ru (84:16, black), (69:31, red), (64:36, green) and (42:58, blue) in the nanocomposites on the TiO₂NT electrodes recorded in O₂-saturated 0.1 M KOH, scan rate of 20 mV/s.

Figure 5.7 Nyquist plots of the TiO₂NT/rGO-PtRu electrodes with their composition of Pt:Ru 84:16 (a), 69:31 (b), 64:36 (c) and 42:58 (d) in the nanocomposites on the TiO₂NT electrodes recorded in O₂-saturated 0.1 M KOH. The amplitude of modulation potential was 5 mV. The frequency was altered, from 100 kHz to 40 mHz with the applied potential of -0.25V. Inset: The corresponding equivalent electric circuit.

Figure 5.8 Amperometric i-t response obtained for ORR at the TiO₂NT/rGO-PtRu electrode with E_{app} of -0.35V in O₂-saturated 0.1M KOH.

List of Tables

Table 1.1 Comparison of technical characteristics of fuel cell technologies.

Table 3.1 Values of elements in an equivalent electric circuit fitted in the Nyquist plots of Figure 3.6

Table 5.1 List of the ORR activities of the fabricated TiO₂NT/rGO-PtRu electrodes.

Table 5.2 Comparison of the onset potential values of different ORR catalysts.

Table 5.3 EIS data of the TiO₂NT/rGO-PtRu electrodes with different compositions of Pt:Ru obtained from the Nyquist plots of Figure 5.4.

List of Abbreviations and Symbols

Abbreviation name

A	Ampere
AFC	Alkaline Fuel Cell
CA	Chronoamperometry
CPE	Constant Phase Element
CV	Cyclic Voltammetry
DEFC	Direct Ethanol Fuel Cell
DFAFC	Direct Formic Acid Fuel Cell
DMFC	Direct Methanol Fuel Cell
E	Potential
EDS	Energy Dispersive Spectroscopy
EIS	Electrochemical Impedance Spectroscopy
j	Current Density
NT	Nanotube
MCFC	Molten Carbonate Fuel Cell
PAFC	Phosphoric Acid Fuel Cell
PEMFC	Proton Exchange Membrane Fuel Cell
SCE	Saturated Calomel Microscopy

SEM	Scanning Electron Microscopy
SOFC	Solid Oxide Fuel Cell
XPS	X-ray Photoelectron Spectroscopy
XRD	X-rayDiffraction

Chapter 1. Electrocatalysis and Fuel cells

1. 1 Introduction

It appears inevitable that the world will face an immense energy crisis in the near future. Moreover, the detrimental effects of environmental pollution that this planet is facing, not only raise concerns in regard to global warming and the manner in which we address it, but also opens new horizons for scientific research in the quest for novel energy sources.^{1,2} Hence, both precautions and remedial measures are required without delay. These concerns have also resulted in the search for alternative power generation sources that provide clean energy, while negating the release of potential environmentally degrading pollutants.^{1,3,4}

The challenge of developing sustainable and renewable energy sources in recent years has led to the technological development of devices for the harnessing of energy and its conversion, encompassing batteries, solar cells, and fuel cells (FCs). Fuel cells have emerged as a promising candidate in the energy field as an electrochemical device, which converts chemical energy contained within different types of fuels into electrical energy with the minimum emission of contaminants. Fuel cells are open thermodynamic systems that are a suitable alternative to conventional electricity generation methods for small-scale applications.⁵ For example, hydrogen and hydrocarbon fuels contain considerable chemical energy, compared to conventional battery materials; therefore, they are currently being widely developed for various energy applications.

Fuel cell technologies are a promising alternative to fossil fuels for supplying energy to rural areas, where there is the lack of access to the public grid. They possess considerably higher cost-effectiveness in contrast with the cost of wiring and the transfer of electricity associated with

conventional power supplies.⁵ Additionally, applications that have fundamentally secure electrical energy requirements may use fuel cells as their primary source of energy.

On the other hand, there exist a number of limitations to the use of fuel cells, which have yet to be overcome. For example, fuel cells are less durable and far less accessible than conventional batteries, and their life spans are directly affected and curtailed by pulse demands.⁶ They have relatively low power densities per unit volume, and gas impurities may have significant detrimental effects on the durability of a particular fuel cell. Though not many notable breakthroughs have been realized to date, significant progress has been made.⁷

1.2 Fuel cell principles

In principle, fuel cells operate in a similar fashion to a traditional batteries; however, fuel cells may supply electricity continuously, so long as fuel is provided, for instance, in the form of hydrogen or methanol.⁸ A fuel cell includes four primary components including an anode, cathode, electrolyte, and an external circuit. For example, in the proton exchange membrane fuel cells (PEMFCs), the oxidation of hydrogen takes place at the anode, whereas the reduction of oxygen occurs at the cathode. Hydrogen and oxygen flow over the electrodes and are converted into water, while generating electricity.⁸ The delivery of electricity is also dependant on the electrolyte solution that is being used. The electrolyte transports either protons or hydroxide ions, whereas the flow of electrons in the external circuit produces an electric current.⁹ Equation 1 and 2 illustrate the reactions that occur at the anode and cathode, respectively:⁵



All fuel cells operate under the same basic principles; however, two of the major differences among fuel cells are the chemical characteristics of the electrolyte and fuel.

1.3 Types of Fuel Cells

There are many types of fuel cells which may be categorized into different groups based on their operating temperature, efficiency, application, and cost.¹⁰ In this section, six main groups will be discussed based on their fuels and electrolytes: (1) phosphoric acid fuel cells (PAFCs); (2) alkaline fuel cells (AFCs); (3) molten carbonate fuel cells (MCFCs); (4) proton exchange membrane fuel cells (PEMFCs); (5) solid oxide fuel cells (SOFCs); and (6) direct methanol fuel cells (DMFCs).¹¹⁻¹³

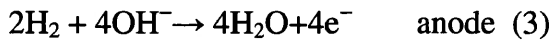
1.3.1 Phosphoric acid fuel cells (PAFC)

PAFCs may employ carbon paper electrodes and a liquid phosphoric acid (H_3PO_4) electrolyte. The operating temperature of PAFCs ranges from 150°C to 220°C as they have low ionic conductivity at low temperatures.⁵ Hydrogen ions (H^+ or protons) function as the charge transfer species, water is produced at the cathode, and platinum is used as a catalyst to speed up the reactions 2 and 3.^{14,15}

The H_3PO_4 electrolyte has long-term stability and lower volatility. Currently, PAFC systems have capacities of up to 200 kW and systems with higher capacities (11 mW) are being tested. It is, however, expensive to fabricate this type of fuel cell due to the platinum catalyst, which is finely dispersed on the electrodes. The electrical efficiency of this type of fuel cells ranges from 40% to 50%, with a Combined Heat and Power (CHP) efficiency of about 85%.^{16,17} PAFC cells may be used for stationary on-site applications.

1.3.2 Alkaline fuel cell (AFC)

The AFC creates electric power by employing an alkaline electrolyte, for example potassium hydroxide (KOH), in the following reactions:^{18,19}



Hydroxyl ions transit through the electrolyte, allowing electrical energy to be extracted.

Recent tests show that AFCs may operate at low temperatures relative to other fuel cells (i.e., between 23°C and 70°C). AFCs also utilize low cost catalysts (i.e., nickel) in both the cathode and anode. Additionally, the electrical efficiency of AFCs is ~60% while the CHP efficiency exceeds 80%.^{20,21} Due to their relatively low efficiency, AFCs are restricted to generating ~ 20 kW.

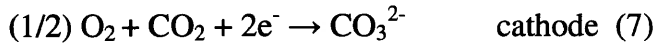
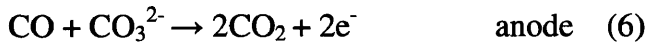
NASA initially used AFCs to provide water and electrical power in the space shuttle, and currently AFCs are widely used in boats, forklifts, and transportation applications.²² AFCs are considered the most efficient and cost-effective fuel cells in that they use nickel as the catalyst and potassium hydroxide as the electrolyte, with a high efficiency of about 70%. Even though AFCs have many advantages they are still impacted by CO poisoning from the hydrogen source, and one major concern relates to finding a substitute for KOH. An additional disadvantage is that AFCs use purified air or pure oxygen, which may increase operational costs.^{5,23}

1.3.3 Molten carbonate fuel cells (MCFC)

MCFCs are applied to many industrial applications. For example, MCFCs have the potential to replace natural gas and coal-based power plants in electrical utilities, and military applications. MCFCs are high-temperature fuel cells that operate between 600 and 700°C. Thus,

most of the characteristics of MCFCs are associated with high operating temperatures. Moreover, they require a long time to attain their operating temperature to generate power.⁵

In this fuel cell, the reaction occurs between hydrogen and carbonate ions to produce CO₂, H₂O, and electrons, as described in the following reactions:



The electrochemical reaction in this kind of fuel cell does not require noble metals or any infrastructure development for installation. A carbonate salt mixture is employed as the electrolyte, and the oxidation process occurs at the anode. The source CH₄, and H₂O are transformed to carbon monoxide (CO), carbon dioxide (CO₂), and hydrogen (H₂). At the cathode, the reaction generates carbonate ions from oxygen (O₂) and CO₂. These carbonate ions are transferred from the cathode to the anode by the electrolyte. Subsequently, the electric current of the cell can be controlled by adjusting the cell voltage.^{5,24}

1.3.4 Proton exchange membrane fuel cell (PEMFC)

The most suitable and commercial application of PEMFs is in transportation (e.g., vehicle engines) as they provide a continuous electrical energy supply at high levels of efficiency and power density.⁵ They can be cost effectively manufactured with longer lifetimes, in comparison to other classes of fuel cells. The current output cost for PEMFCs is estimated to be from \$500 to \$600 per kW.^{25,26}

In PEMFCs, a stream of hydrogen is delivered to the anode side of the membrane electrode assembly (MEA). At the anode side, the hydrogen is catalytically cleaved into protons

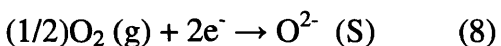
and electrons, which is represented by eq (1). This oxidation half-cell reaction or Hydrogen Oxidation Reaction (HOR) is represented by eq (2).

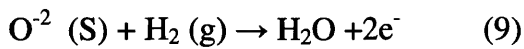
The newly formed protons permeate through the polymer electrolyte membrane to the cathode side, whereas the electrons travel along an external load circuit to the cathode side of the MEA, thus creating the current output of the fuel cell. Meanwhile, an oxygen stream is delivered to the cathode side of the MEA, where oxygen molecules react with protons that permeate the polymer electrolyte membrane, and the electrons arriving through the external circuit form water molecules. This reduction half-cell reaction, or oxygen reduction reaction (ORR) is represented by eq. 2.

PEMFCs operate within a temperature range between 60 to 100 °C. By increasing the temperature, the efficiency may be raised through an increase in the reaction rate. However, should the temperature be raised above 100 °C (boiling point), the water within the cell will evaporate, which decreases the conductivity of the membrane, thereby reducing the efficiency of the cell. At optimal temperatures, the electrical efficiency of PEMFC cells is between 40% and 50%, with an output power of ~250 kW.²⁷⁻²⁹

1.3.5 Solid oxide fuel cell (SOFC)

SOFCs are high temperature fuel cells that contain an electrolyte of solid metallic oxide ceramic. SOFCs utilize a mixture of hydrogen and carbon monoxide, which is made by repairing hydrocarbon fuel and air as the oxidant in the fuel cell.³⁰ Yttria stabilized zirconia (YSZ) is typically used as an electrolyte due to its high chemical and thermal stability, and pure ionic conductivity.^{31,32} At the cathode, oxygen is reduced at high temperature (e.g., 1000 °C).⁵ At the anode, fuel oxidation is described by the following reactions:





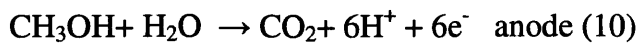
SOFCS are ideally suited for large scale distributed power generation systems that require a capacity of hundreds of MWs. SOFCs are reliable modular systems, with fuels that are flexible with low harmful (NOx and SOx) gas emissions.⁵ This system operates without noise and has minimal maintenance costs; however, there are some limitations in using SOFCs, including extended start-up and cool down times as well as high operating temperatures. There is ongoing research to find possible solutions to these issues such that SOFCs may be more easily applied for energy production.³³

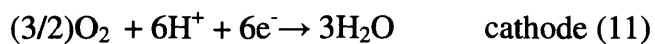
1.3.6 Direct methanol fuel cells (DMFCs)

Methanol is considered to be the best fuel after hydrogen in terms of energy density and it exhibits several benefits over the use of hydrogen. For example, methanol, which is derived from wood alcohol, is cheap, plentiful, and renewable, and is in liquid form, hence it is easy to store, transport, and distribute.^{12,34}

DMFCs are an advanced type of PEMFC that are considered to be one of the most promising power sources due to their low operating temperatures, extended longevity, and rapid refueling capabilities.^{5,34} Furthermore, they do not require recharging, and are a clean renewable energy source. For these reasons, the use of methanol as electrochemical fuel decreases the difficulty in constructing an energy conversion system, by reducing complexity and cost.^{5,34}

The primary fuel source in DMFC systems is methanol, which is broken down into CO₂, H⁺, and e⁻ at the anode, whereas water is formed at the cathode using oxygen that is available in ambient air.⁵ These reactions are described in eq. 10 and 11:





cathode (11)

DMFC systems are configured as active and passive⁵, where active DMFCs are high efficiency systems that include a methanol feed pump, CO₂ separator, fuel cell stack, methanol sensor, circulation pump, as well as pump drivers and controllers. Active DMFCs are generally applied to control applications for quantities such as flow rate and temperature, whereas in passive DMFC systems, the methanol pumping devices and external process for blowing air into the cell are eliminated. Thus, ambient oxygen is defused by an air breathing feature of the cell into the cathode.³⁴ Rather than actively pumping methanol, the passive system uses a concentration gradient to drive the diffusion of methanol within the cell.³⁴ Finally, passive systems function better as they are cost effective, simply constructed, and are capable of sustained operation despite significant reductions in parasitic power loss and system volumes.^{5,34}

In DMFCs, methanol is applied as either a vapour or liquid, albeit vapour is ideal due to its voltage and power density. Liquid methanol does not adapt for mass transfer and requires high localized cooling at the anode.⁵ Moreover, at the electrocatalyst surface, vapourized methanol crossover, from anode to cathode, confers higher performance in comparison to liquid methanol. However, there are some downsides inherent to vapour feed cells.³⁵ For example, vapourized methanol dehydrates membranes, has a shorter lifetime, and higher temperatures are required for fuel vaporization.³⁵ As a result, they require more complex and costly designs. In addition, they are not appropriate for portable applications.

A core component in DMFCs is a proton exchange membrane (PEM), which can extend low penetrability and high proton conductivity. It may also provide chemical stability, and high thermal tolerance toward the development of ideal DMFCs. Hydrophobic ion exchange polymers are required as the performance of PEM may be negatively impacted by water and methanol,

which adsorbs to the acidic membranes.^{36,37} Moreover, the sulfonation of the composite PEM via the incorporation of inorganic-ceramic materials can help to overcome water and methanol adsorption.^{38,39}

In summary, fuel cells have many applications due to their wide range of power, from 1 to 10 mW.⁵ They may be flexibly integrated into compact devices such as mobile phones, and larger systems such as vehicles. Fuel cells are also commonly used in distributed power systems and grid-quality AC. Table 1.1 summarizes various fuel cell features and applications.⁵

Fuel cell type	Operating Temperature (°C)	System Output (kW)	Electrical Efficiency (%)	Combined Heat and Power (CHP) Efficiency	Applications	Advantages
Akaline (AFC)	90-100	10-100	60	> 80	Military Space	<ul style="list-style-type: none"> Cathode reaction faster in alkaline electrolyte, leads to higher performance Can use a variety of catalysts
Phosphoric Acid (PAFC)	150-200	50-100	>40	>85	Distributed generation	<ul style="list-style-type: none"> Higher overall efficiency with CHP Increased tolerance to impurities in hydrogen
Solid Oxide (SOFC)	600-1000	<1-3000	35-43	<90	Auxiliary power Electric Utility Large distributed generation	<ul style="list-style-type: none"> High efficiency Fuel flexibility Can use a variety of catalysts Solid electrolyte reduces electrolyte management problems Suitable for CHP Hybrid/GT cycle
Molten Carbonate (MCFC)	600-700	<1-1000	45-47	>80	Electric utility Large distributed generation	<ul style="list-style-type: none"> High efficiency Fuel flexibility Can use a variety of catalysts Suitable for CHP
Polymer Electrolyte Membrane (PEM)	50-100	<1-250	53-58	70-90	Backup power Portable power Small distributed generation Speciality vehicle Transportation	<ul style="list-style-type: none"> Solid electrolyte reduces corrosion & electrolyte management problems Low temperature Quick start-up
Direct methanol fuel cell (DMFC)	60-200	0.001-100	40	80	Replace batteries in mobiles; computers and other portable devices	<ul style="list-style-type: none"> Reduced cost due to absence of fuel reformer

Table 1.1 summarizes fuel cell features and applications.⁵

1.4 Anodic electrocatalysts for DMFCs

Catalyst loading plays a significant role in the fabrication of DMFCs for optimum performance. There are some catalyst loading processes that have employed sputtering, screen printing, spraying, decaling, and electrodeposition.⁴⁰ Noble metals are commonly used as anodic catalysts. For example, the high stability of Pt in acidic electrolytes provides some advantages in fuel cell applications.⁴⁰ However, Pt is expensive and easily poisoned by oxidation intermediates, namely CO_{ads} that are generated by cell reaction processes.^{41,42} The poisoning of Pt by CO reduces the efficiency of the oxidation process and blocks the adsorption of methanol on electrode sites. Possible solutions to improve using Pt as catalyst include reducing the loading amount while saving the same level of activity by applying appropriate synthetic strategies.⁴⁰ In addition, new catalyst formulations should have the capacity to promote the complete combustion to CO₂.⁴⁰⁻⁴²

1.4.1 Pt catalysts based nanostructured materials for DMFCs

Active metal are distributed supports to increase the active metal area and population of active sites on the surface. It is recognized that the surface properties of supported metallic systems are affected by the morphologies and dimensions of the supported metals, as well as the nature of the supports.^{40,43} When support metals shrink to the nanoscale, dimensional variabilities may be exploited for charge transfer processes.⁴⁰ For example, the use of nanoparticles may be limited due to their potential for aggregation; the effective electrochemical surface area (ECSA) can be reduced; and the large number of nanoparticle/nanoparticle interfaces may hinder mass diffusion and efficient charge transfer.^{44,45} It has been observed that catalysts with one-dimensional nanostructures (e.g., nanowires (NWs) or nanotubes (NTs)) are more efficient than three-dimensional nanoparticles. Hence, all limitations may be avoided through the provision of a

high catalytic surface area that does not require a large surface area support.⁴⁴⁻⁴⁶ For example, when the tobacco mosaic virus (TMV) is employed as a Pt NT template, it provides an electrochemically active surface area that is four to eight fold more extensive than similarly sized Pt NPs.^{40,47} However, as Pt is readily poisoned by CO, the combination of Pt with metals such as Fe, Cr, Sn, Os, Mo, Ti, Re, Ru, and Ta, has the potential to reduce poisoning and expand the reactivity of Pt in the oxidation of methanol.⁴⁰

1.4.2 Pt-Ru catalysts for DMFCs

Bimetallic (Pt/Ru) systems present a potential solution for overcoming the CO poisoning of active sites. The anti-poisoning capacity of Pt/Ru results from OH groups that are created on Ru sites.⁴⁰ Ru(Pt)₂COH is one of the species that has been proposed by the sequential dehydrogenation of methanol. The electrochemical study of CO has produced evidence that PtRu domain sites are responsible for providing the higher activity of the system.^{40,48} Surface oxidic species on Ru might be an additional feature that accounts for the higher activity.^{40,49}

1.4.3 Pt-Sn catalysts for DMFCs

Pt-Sn catalysts can exhibit good and poor activity.^{40,50,51} It is likely that Sn adsorbed on Pt provides good activity for methanol oxidation; however, Pt-Sn as an alloy may exhibit poor activity.⁵² Indeed, surface concentrations of Sn participates with influencing activity, and this activity is related to the electrical potential.^{40,53,54}

1.4.4 Catalysts based on metal oxide supports (effect of RuO₂)

The effect of RuO₂ on the oxidation of methanol on Pt surfaces has been studied over the past few decades.^{40,55-58} Crystalline RuO₂ substantially improves the oxidation of methanol by Pt nanoparticles. The higher activity of the crystalline RuO₂ phase is responsible for the

improvement to a higher degree than metallic Ru toward the oxidation of CO through the formation of Ru-OH on the surface.^{40,59} Moreover, hydrous RuO₂ can provide the need of hydroxide species to facilitate CO oxidation on Pt sites, and thus enhance catalytic properties. Rolison et al. found that a commercial Pt–Ru catalyst that contained Pt and Ru oxides could control the chemical state of Ru to favour RuO_xH_y over metallic Ru.^{56,60}

1.4.5 Effect of TiO₂

TiO₂ has the capacity to substantially enhance methanol oxidation on both Pt and Pt-Ru nanoparticle surfaces.^{61,62,63} TiO₂ may be prepared from the hydrolysis of organic Ti, or an organic Ti salt, and is also stable in acidic solutions. If TiO₂ is incorporated into electrodes as a base for Pt, it will alter the electronic properties of the Pt surface due to strong interactions between TiO₂ and Pt, resulting in weak chemical adsorption on the surface of electrode.⁴⁰

1.4.6 Effect of IrO₂

IrO₂ has been studied as a support for Pt-Ru nanoparticles in catalysts to enhance methanol oxidation.^{40,64} The advantage of Ru in catalysts is that it can decrease the oxidation potential of CO_{ads}, which improves methanol oxidation activity. Using Ir-IrO₂ as a catalyst support enhances activity more than commercial Pt-Ru catalysts due to the ease of formation of hydroxyl groups on IrO₂ at lower potentials.^{40,65}

1.5 Electrocatalyst for oxygen reduction reaction (ORR) in FCs.

Fuel cells are clean and highly efficient, hence they are recognized as an environmentally friendly power source.⁶⁶⁻⁶⁹ The oxygen reduction reaction (ORR) at the cathode is considered as the primary factor in scrutinizing the performance of a fuel cell. The commercial catalyst used in ORR is Pt, which can effectively simplify the reaction.⁶⁸ Pt-based electrocatalysts present

significant cathodic current densities and low overpotentials. However, the extensive application of Pt as an electrocatalyst toward ORR is hindered by its high cost and sluggish kinetics.⁶⁹ Unfortunately, Pt is unstable as an electrocatalyst in ORR due to electrochemically active surface area loss subsequent to long use.⁶⁶⁻⁶⁹ This loss of Pt electrocatalytic surface area decreases the activity of ORR, such that it impacts the overall performance of the fuel cell.⁶⁶⁻⁶⁹ Not only can Pt affect the activity of ORR, it is also an expensive metal. In order to enhance ORR activity and reduce the cost of catalysts, the preparation of Pt with other noble or transition metals has been studied, for example: Au, Pd, rGO, Fe, Co.⁶⁶⁻⁶⁹

1.5.1 Au toward ORR

Platinum has been used as a cathodic catalyst in PEMFCs with a phosphoric acid electrolyte and (PA)-dopedpolybenzimidazole (PBI) membrane,⁶⁹ which gave rise to large cathodic current densities and low overpotentials. However, in this reaction, as cathodic electrocatalyst, Pt has faced problems.⁶⁹ The significant degradation of the PA-impregnated membrane through the strong adsorption of phosphate on the Pt surface, acts to block catalytically active sites.⁶⁹ Thus, including a material, such as Au, that is inert in the bulk state and has high catalytic activity at the nanoscale has been explored to attenuate the degradation the PA-impregnated membrane.

Phosphate species such as H_3PO_4 , H_2PO_4^- , HPO_4^{2-} , and PO_4^{3-} -ions adsorb to Pt surfaces, where H_2PO_4^- ions comprise the strongest adsorbate on the Pt surface.⁶⁹ In contrast, there are a various adsorptive phosphate species behaviors on Au surfaces. Indeed Habib et al. carried out a Fourier-transform infrared (FTIR) study of the adsorption from aqueous solutions of phosphoric acid onto Pt and Au surfaces, under a variety of concentrations and potentials.^{69,70} The result showed that molecular H_3PO_4 was more highly adsorbed on the Au surface than on the Pt surface in acidic

solutions.⁶⁹⁻⁷¹ Pt-Au can resolve the problem of Pt initiated catalyst poisoning by CO-like species through changing the electronic band structure of Pt by modifying the surface adsorption strength, and increasing the electrochemically active surface area of Pt, which is a major factor toward the improvement of the catalytic performance and efficiency of Pt catalysts. Pt-Au has been considered as an attractive material for improving the activity and stability of Pt catalysts for the oxygen reduction reaction.^{69,70}

1.5.2 Pd toward ORR

Since Pt electrocatalysts suffer from poor reaction kinetics and poisoning, Pt-Pd have wide applications in electrocatalytic reactions.⁷² Of all the atomic metals, Pd is considered the best candidate for the formation of bimetallic nanocrystals with Pt, due to the properties that both metals share, such as identical face-centered-cubic (fcc) structures and almost identical lattice constants. Additionally, Pd is less expensive than Pt, and device cost can be reduced even further by applying Pd as the base metal. The introduction of Pd may save the electrocatalysts from degradation to some degree. The stability of the Pt-Pd electrocatalyst is significantly improved as adding Pd to Pt shifts the dissolution potential of Pt.⁷² The integration of Pd and Pt promotes their catalytic performance and even extends their potential applications.

1.6 Scope of this thesis

The primary intent of this M.S.c thesis was to synthesize Ir-, Ru- and Pt-based nanomaterials, and to study their electrochemical properties for fuel cell applications. The first objective of this research was to decrease the cost and the amount of the electro-catalysts, required in the current application by applying an alternative metal with a lower price. One goal of this research included the development of new synthesis techniques that generated a high catalytic surface area for both methanol oxidation applications, and oxygen reduction reactions.

By increasing the ratio or volume for the alternate catalyst, it can greatly increase the active surface area, which will lead to a decrease in the material cost. The second goal of this thesis was to address the use of Pt as an electrocatalyst, which has an issue that requires solving; namely poisoning species. The scope of this thesis to investigate the effect of Ir or Ru on Pt based nanomaterial catalysts with high electrocatalytic activity toward the oxidation of methanol and oxygen reduction reactions. Modification techniques for both catalysts and supports were investigated in order to develop efficient PtIr, and PtRu based nanomaterials.

In the following chapter, experimental methods will be provided as relates to the fabrication of nanostructured materials, as well as the techniques that were employed to analyze their structures. Chapter 3 details the results of the electrochemical study of Pt-Ir nanoparticles deposited on TiO₂NTs for methanol oxidation. Chapter 4 presents the electrocatalytic properties of Pt-Ru nanoparticles deposited on TiO₂NTs toward methanol oxidation. The modification of TiO₂NT with PtRu/GO nanocomposites for improved oxygen reduction reactions is discussed in Chapter 5. Finally, Chapter 6 will provide a summary of results and anticipated future work.

References

- (1) Dutta, K.; Das, S.; Rana, D.; Kundu, P.P. *Taylor & Francis*. **2015**, *55*, 1.
- (2) Cox, P. M.; Betts, R. A.; Jones, C. D.; Spall, S. A.; Totterdell, I. J. *Nature*. **2000**, *408*, 184.
- (3) Lovley, D. R. *Current Opinion in Biotechnology*. **2006**, *17*, 327.
- (4) Davis, F.; Higson, S. P.J. *Biosensors and Bioelectronics*. **2007**, *22*, 1224.
- (5) Mekhilefa, S.; Saidurb, R.; Safari, A. *Renewable and Sustainable Energy Reviews*. **2012**, *16*, 981.
- (6) Pollet, B.G.; Staffell, I.; Shangc, J.L. *Electrochimica Acta*. **2012**, *84*, 235.

- (7) Merle, G.; Wessling, M.; Nijmeijer, K. *Journal of Membrane Science*. **2011**, *377*, 1.
- (8) The principle of fuel cells: *Functional Membranes and Plant Technology*; 2015. Available online at: <http://www.fumatech.com/EN/Fuel-cells/Principle-of-fuel-cells/>
- (9) Mark Ormerod, R. *Chem Soc Rev*. **2003**, *32*, 17.
- (10) Kirubakaran, A.; Jain, S.; Nema, RK. *Renew Sustain Energy Rev*. **2009**, *13*, 243.
- (11) Nguyen, T.H.; Fraiwan, A.; Choi, S. *Biosensors and Bioelectronics*. **2014**, *54*, 640.
- (12) Giorgi, L.; Salernitano, E.; Dikonimos Makris, T.; Gagliardi, S.; Contini, V.; De Francesco, M. *International Journal Of Hydrogen Energy*. **2014**, *39*, 21601.
- (13) García-Camprubí,M.;Izquierdo,S.;Fueyo,N. *Renewable and Sustainable Energy Reviews*. **2014**, *33*, 701.
- (14) Phosphoric acid fuel cell. Irvine: *National Fuel Cell Research Centre*, University of California; 2009. Available online at: <http://www.nfcrc.uci.edu/>
- (15) Phosphoric acid fuel cell, Wikipedia, the free encyclopaedia. Available online at: http://en.wikipedia.org/wiki/Phosphoric_acid_fuel_cell [accessed 12.01.10].
- (16) Phosphoric acid fuel cell (PAFC). *The U.S. Department of Defense (DoD) Fuel Cell Test and Evaluation Centre (FCTec)*, 2010. Available online at: http://www.fctec.com/fctec_about.asp.
- (17) Remick, RJ.; Wheeler, D.; Singh, P. MCFC and PAFC R&D workshop summary report. U.S. Department of Energy; 13 January **2010**.
- (18) Alhassan, M.; Garba, MU.; Design of an alkaline fuel cell. Minna: Federal University of Technology; **2006**.
- (19) Redox reaction, Wikipedia, the free encyclopaedia. Available online at: http://en.wikipedia.org/wiki/Redox_reaction [accessed 04.04.10].

- (20) Crawley G. Fuel cell today. Johnson Matthey Plc. 04241894; 2006, March. Available online at: <http://www.fuelcelltoday.com>.
- (21) Comparison of fuel cell technologies. *US Department of Energy Hydrogen Program*. Available online at: <http://www.hydrogen.energy.gov> [accessed December 2008].
- (22) Kordesch, K. Alkaline fuel cells applications, innovative energy technology. Austria: Institute of High Voltage Engineering, U Graz; **1999**.
- (23) Larminie, J.; Dicks, A. Fuel cell system explained. 2nd ed. United Kingdom: John Wiley & Sons; **2003**
- (24) Chudej, K.; Bauer, M.; Pesch, HJ.; Schittkowski, K. Numerical simulation of a molten carbonate fuel cell by partial differential algebraic equations. Universität Bayreuth; **2008**.
- (25) Sopian, K. Challenges and future developments in proton exchange membrane fuel cells. Elsevier Ltd.; **2005**.
- (26) Therdthianwong, A.; Saenwiset, P.; Therdthianwong, S. Cathode catalyst layer design for proton exchange membrane fuel cells. *Fuel*, in press, Corrected Proof, Available online 21 July **2011**.
- (27) Yu, K.; Groom, D.J.; Wang, X.; Yang, Z.; Gummalla, M.; Ball, S.C.; Myers, D.J.; Ferreira, P.J. *Chem. Mater.* **2014**, *26*, 5540.
- (28) Rowshanzamir, S.; Peighambarioust, S.J.; Parnian, M.J.; Amirkhanlou, G.R.; Rahnavard, A. *international journal of hydrogen energy*. **2015**, *40*, 549.
- (29) Kraytsberg, K.; Ein-Eli, Y. *Energy Fuels*. **2014**, *28*, 7303.
- (30) Mark, O.R. *Chem. Soc. Rev.* **2003**, *32*, 17.
- (31) Will, J.; Mitterdorfer, A.; Kleinlogel, C.; Perednis, D.; Gaukler, L.J. *Solid State Ionics*. **2000**, *131*, 79.
- (32) Singhal, S.C. *Solid State Ionics*. **2000**, *135*, 305.

- (33) Tanaka, K.; Wen, C.; Yamada, K. *Fuel*. **2000**, *12*, 1493.
- (34) Dang, L.Q.; Nguyen, M.T.; Nguyen, V.L.; Cao, M.T.; Lê, V.T.; Nguyen, L.H.; Nguyen, N.P.; Nguyen, T.H.; Do, T.N. *Adv. Nat. Sci.: Nanosci. Nanotechnol.* **2014**, *5*, 035015.
- (35) Scott, K.; Taama, W.M.; Argyropoulos, P. *J Power Sources*. **1999**, *79*(1), 43.
- (36) Hatanaka, T.; Hasegawa, N.; Kamiya, A.; Kawasumi, M.; Morimoto, Y.; Kawahara, K. *Fuel*. **2002**, *81*, 2173–6.
- (37) Kreuer, KA. *J Membr*, **2001**, *185*(1), 29.
- (38) Silva, V.; Ruffmann, B.; Silva, H.; Mendes, A.; Madeira, M.; Nunes, S. *J Electrochim.* **2006**, *51*, 3699.
- (39) Silva, VS.; Weisshaar, S.; Reissner, R.; Ruffman, B.; Vetter, S.; Mendes, A.; et al. *J Power Sources*. **2005**, *145*(2), 485.
- (40) Kakati, N.; Maiti, J.; Lee, S.H.; Jee, S.H.; Viswanathan, B.; Yoon, Y.S. *Chem. Rev.* **2014**, *114*, 12397.
- (41) Zhao, J.; He, X.; Tian, J.; Wan, C.; Jiang, C. *Energy Convers. Manage.* **2007**, *48* (2), 450.
- (42) Sundmacher, K.; Schultz, T.; Zhou, S.; Scott, K.; Ginkel, M.; Gilles, E. D. *Chem. Eng. Sci.* **2001**, *56* (2), 333.
- (43) Aricò, A. S.; Srinivasan, S.; Antonucci, V. *Fuel Cells*. **2001**, *1*(2), 133.
- (44) Chen, Z.; Waje, M.; Li, W.; Yan, Y. *Angew. Chem., Int. Ed.* **2007**, *46*, 4060.
- (45) Choi, S. M.; Kim, J. H.; Jung, J. Y.; Yoon, E. Y.; Kim, W. B. *Electrochim. Acta*. **2008**, *53*, 5804.
- (46) Lee, E. P.; Peng, Z.; Chen, W.; Chen, S.; Yang, H.; Xia, Y. *ACS. Nano.* **2008**, *2*, 2167.
- (47) Górzny, M. Ł.; Walton, A. S.; Evans, S. D. *Adv. Funct. Mater.* **2010**, *20*, 1295.
- (48) Dinh, H. N.; Ren, X.; Garzon, F. H.; Zelenay, P.; Gottesfeld, S. *J. Electroanal. Chem.* **2000**, *491*, 222.

- (49) Arico, A. S.; Creti, P.; Modica, E.; Monforte, G.; Baglio, V.; Antonucci, V. *Electrochim. Acta*. **2000**, *45* (25–26), 4319.
- (50) Wang, K.; Gasteiger, H. A.; Markovic, N. M.; Ross, P. N., Jr. *Electrochim. Acta*. **1996**, *41* (16), 2587.
- (51) Wei, Z.; Guo, H.; Tang, Z. *J. Power Sources*. **1996**, *58* (2), 239.
- (52) Wasmus, S.; Kuver, A. *J. Electroanal. Chem.* **1999**, *461*, 14.
- (53) Markovic, N. M.; Widelov, A.; Ross, P. N.; Monteiro, O. R.; Brown, L. G. *Catal. Lett.* **1997**, *43* (3–4), 161.
- (54) Abdel Rahim, M. A.; Khalil, M. W.; Hassan, H. B. *J. Appl. Electrochem.* **2000**, *30*(10), 1151.
- (55) Chen, Z.; Qiu, X.; Lu, B.; Zhang, S.; Zhu, W.; Chen, L. *Electrochim. Commun.* **2005**, *7* (6), 593.
- (56) Profeti, L. P. R.; Profeti, D.; Olivi, P. *Int. J. Hydrogen Energy*. **2009**, *34*, 2747.
- (57) Pietron, J. J.; Pomfret, M. B.; Chervin, C. N.; Long, J. W.; Rolison, D. R. *J. Mater. Chem.* **2012**, *22*, 5197.
- (58) Ma, J.-H.; Feng, Y.-Y.; Yu, J.; Zhao, D.; Wang, A.-J.; Xu, B.-Q. *J. Catal.* **2010**, *275*, 34.
- (59) Huang, S.-Y.; Chang, C.-M.; Wang, K.-W.; Yeh, C.-T. *ChemPhysChem*. **2007**, *8*, 1774.
- (60) Cao, L.; Scheiba, F.; Roth, C.; Schweiger, F.; Cremers, C.; Stimming, U.; Fuess, H.; Chen, L.; Zhu, W.; Qiu, X. *Angew. Chem., Int. Ed.* **2006**, *45*, 5315.
- (61) Hirakawa, K.; Inoue, M.; Abe, T. *Electrochim. Acta*. **2010**, *55*, 5874.
- (62) Tian, J.; Sun, G.; Jiang, L.; Yan, S.; Mao, Q.; Xin, Q. *Electrochim. Commun.* **2007**, *9*, 563.
- (63) Lee, J.-M.; Han, S.-B.; Kim, J.-Y.; Lee, Y.-W.; Ko, A.-R.; Roh, B.; Hwang, I.; Park, K. *W. Carbon*. **2010**, *48*, 2290.

- (64) Jian, X.-H.; Tsai, D.-S.; Chung, W.-H.; Huang, Y.-S.; Liu, F.-J. *J. Mater. Chem.* **2009**, *19*, 1601.
- (65) Baglio, V.; Amin, R. S.; El-Khatib, K. M.; Siracusano, S.; D'Urso, C.; Aricò, A. S. *Phys. Chem. Chem. Phys.* **2014**, *16*, 10414.
- (66) Liua, J.; Zhaoa, Q.; Lia, X.; Chen, J.; Zhangc, D. *Applied Catalysis B: Environmental.* **2015**, *165*, 519.
- (67) Bezerra, C.W.B.; Zhang, L.; Lee, K.; Liu, H.; Marques, A.L.B.; Marques, E.P.; Wang, H.; Zhang, J. *Electrochimica Acta*, **2008**, *53*, 4937.
- (68) Wang, B. *Journal of Power Sources*, **2005**, *152*, 1.
- (69) Lima, J-E.; Leea, J.; Sang, H-A.; Cho, E.; Kim, H-J.; Jong, H-J.; Sona, H.; Kima, S-K. *Applied Catalysis B: Environmental.* **2015**, *165*, 495.
- (70) Habib, M.A.; Bockris, J.O'M. *J. Electrochem. Soc.* **1985**, *132*, 108.
- (71) Niaura, G.; Gaigalas, A.K.; Vilker, V.L. *J. Phys. Chem. B*, **1997**, *101*, 9250.
- (72) Li, S-S.; Lv, J-J.; Teng, L-N.; Wang, A-J.; Chen, J-R.; Feng, J-J. *ACS Appl. Mater. Interfaces.* **2014**, *6* (13), 10549.

Chapter 2 Experimental Methods

2.1 Introduction

The objectives for the study of PtIr, PtRu, and PtRu-rGO based nanomaterials as electrocatalysts, which may be applied in methanol based fuel cells, were described in the previous chapter, as well as a discussion of the challenges that must be overcome toward their commercial application. In this chapter, the primary experimental methodologies and techniques employed in this M.Sc. project will be introduced. Details related to the experimental procedures and equipment, which pertain to each specific study, are presented in Chapters 3 - 5.

2.2 Chemicals and Materials

The chemicals used in this research included sulfuric acid (99.999%); hydrochloric acid (37.5%); sodium borohydride ($\geq 98\%$); potassium hydroxide ($\geq 85\%$); dimethyl sulfoxide (DMSO) (99.99%); hydrofluoric acid (50%); and methanol, which were purchased from Sigma-Aldrich. Titanium wire (99.7%, 2mm diameter); titanium plates (99.2%) (cut into 1.25cm \times 0.8cm rectangles with a thickness of 0.5cm); Pt wire (99.9%, 0.5mm diameter); H₂PtCl₆.6H₂O (99.9%); RuCl₃.XH₂O (99.9%); and IrCl₃ (99.9%), were purchased from Alfa-Aesar.

The gases utilized for this thesis project were argon (PPAXAIR, UHP 99.99%); carbon monoxide (PRAXAIR, Grade 2.5, 99.5%); and oxygen.

Pure water (18.2 M Ω cm), obtained from a NANOpure® Diamond™ UV ultrapure water purification system, was used for cleaning purposes and in the preparation of all solutions and electrolytes.

2.3 Fabrication of nanomaterials

2.3.1 Ti-etched electrode.

The nanostructures that were used as electrodes in the Direct Methanol Fuel Cell studies (Chapter 3,4,5,6) were grown directly onto Ti plates using an electrochemical reduction method. Ti strips (99.2%, 1.25cm \times 0.80 cm \times 0.5mm) were cleaned via sonication in acetone followed by rinsing with pure water (18M Ω cm).¹ The Ti substrates were etched in an 18 wt % HCl solution at 85 °C for 30 min., and then finally rinsed with pure water.

2.3.2 TiO₂ nanotube supported nanoparticles

TiO₂ NTs were fabricated in a two-electrode electrochemical cell¹ using an etched Ti plate as the working electrode, which was rinsed with pure water. A Pt wire coil (5.0 cm²), which was cleaned prior to each experiment via flame-annealing, was applied as counter electrode. The anodization took place in a solution that contained dimethyl sulfoxide (DMSO) with 2% (wt) HF and 2% (wt) H₂O under 40 V for eight hours. Finally, the sample was rinsed with pure water and then heated to 450 °C for three hours to generate the anatase structured TiO₂ NTs.

TiO₂ supported nanoparticles were used for direct methanol fuel cells (DMFC) (Chapters 3 - 5). An ultraviolet light irradiation method was applied to enhance the activity of the TiO₂NT supports.² To activate the sample with UV pretreatment methods, a TiO₂ sample was placed in a quartz tube that contained 50% methanol-H₂O (v/v). TiO₂ was then bubbled with Ar for 20 minnutes; after which the quartz tube was capped and irradiated under the intense UV light for one hour.

All of the TiO₂NT supported samples were prepared using a facile room temperature impregnation method with different reduction techniques: chemical reduction by NaBH₄ (Chapter 3 & 4), and electrochemical reduction through the application of potential (Chapter 5). Firstly, for

chemical reduction (Chapters 3-4), all treated TiO₂ was prepared at room temperature with NaBH₄ as the reducing agent. The appropriate volumes of metal and water were combined and sonicated for 20 minutes. The PtIr, and PtRu- containing coating solution (20 μL) was applied directly to the surfaces of the TiO₂NT electrode. Following this, 1M NaBH₄ was added to the surface solution and allowed to sit for 10 minutes. When the electrodes are completed, they were rinsed with pure water, and then dried. This method was repeated three times to obtain the desired coating amount.

Secondly, for electrochemical reduction (Chapter 5), PtRu nanoparticles with GO were electrochemically deposited on treated TiO₂NTs. The appropriate metal precursors were prepared and sonicated for 20 minutes. The PtRu-rGO solution (100 μL) and 0.5M H₂SO₄ (20ml) were combined in a beaker and sonicated for 20 minutes, and then introduced into the cell. The electrochemical reduction was carried out by applying a potential of -1.0V (vs Ag/AgCl) over 1000 seconds. . The completed electrodes were then rinsed with ultrapure water and allowed to dry. This procedure was applied for different electrode compositions.

2.4 Surface Analysis

The surface morphologies of different nanocompositions, which were supported by TiO₂NT, were characterized by a scanning electron microscope (SEM) using a Hitachi Su-70 Schott Field Emission SEM, and X-ray energy dispersive spectrometry (EDX), which recorded the elemental mapping with the application of 15 kV.

The synthesized nanomaterials were analyzed via X-ray diffraction (XRD) and X-ray photoelectron spectroscopy (XPS). XRD patterns were recorded using a Philips PW 1050-3710 diffractometer with a CU Kα(λ= 1.5405) radiation source, while the XPS was addressed using a Thermo Scientific K-Alpha XPS spectrometer. Samples were run at a take-off angle (relative to

the surface) of 90°. A monochromatic Al K α X-ray source worked with a spot area of 40 μ m. The position of energy scale was modified to place the main C 1s feature (C-C) at 284.6 eV. XPSpeak software was employed to process all data.

2.5 Electrochemical experiments

Two electrochemical workstations, VoltaLab PGZ301 and CHI 660B, were utilized in this research, and a three-electrode cell system was employed. The reference electrode was comprised of a silver-silver chloride (Ag/AgCl) 1.0 M KCl electrode. The counter electrode was a Pt wire coil, which was cleaned prior to each experiment by flame annealing, and then rinsed with pure distilled water. The working electrode consisted of nanoparticle materials, which were prepared on either TiO₂NTs or Ti substrate. For several of the experiments, prior to conducting the electrochemical studies, the passage of ultrapure argon gas continued through the electrolyte solution (H₂SO₄, H₂SO₄+CH₃OH, KOH) for approximately 15 minutes to remove all dissolved oxygen. In other experiments, O₂ gas was purged from, or introduced into the solution to obtain an O₂-saturated solution³, which also ran continuously above the solution during the electrochemical studies. All experiments were conducted at room temperature (20 ± 2°C), and data acquisition and analysis were performed using VoltaMaster 4 software.

2.6 Summary

This chapter served to introduce the materials that were employed in the research for this M.Sc thesis project. The experimental methods and equipment employed for the synthesis and characterization of PtIr, PtRu, and PtRu-rGO based nanomaterials were outlined. More experimental details as well as the characterization and electrocatalytic activity of prepared PtIr, PtRu and PtRu-rGO nanomaterials will be presented in the following three chapters.

References

- (1) Tian, M.; Malig, M.; Chen, S.; Chen,A. *Electrochem.Commun.* **2011**, *13*, 370.
- (2) Tian, M.; Thind,S.S.; Chen, S.; Matyasovsky, N.; Chen, A. *Electrochem.Commun.* **2011**, *13*, 1186.
- (3) Govindhan, M; Chen, A. *J. Power Sources* **2015**, *274*, 928

Chapter 3 Synthesis and electrochemical study of Pt-Ir nanoparticles deposited on TiO₂NTs for methanol oxidation

3.1 Introduction

Direct methanol fuel cell (DMFC) comprises a promising future energy technology alternative to conventional energy generating devices due to its negligible pollutant emissions, highly efficient energy conversion, ease of distribution, abundant availability of methanol fuel, and its high energy density.¹ Though Pt is traditionally employed as an active catalyst in DMFC, it is an expensive metal, and the performance of pure Pt electrodes is diminished by partial oxidation products (ie. CO) in the methanol oxidation reaction.² Increasing the efficacy of fuel cells is one of the significant challenges that electrochemistry has undertaken. These efforts have initiated research into bimetallic catalysts, incorporating elements such as Ru, Ir, Sn, W, Mo. Iridium has been selected as the precious metal of choice for this research due to its positive attributes, which encompass excellent corrosion resistance in acidic media, good electrical conductivity, and high electrocatalytic activity.³⁻⁵ TiO₂ is chosen as a support for noble metal nanomaterials in this study due to its high stability, chemical inertness, low cost, non-toxicity and high surface area. However, TiO₂NT is a semiconductor, and has low conductivity.⁴ In the present research, we modified TiO₂NTs with PtIr nanoparticles. By incorporating Ir, it is expected the electrocatalytic activity and CO tolerance of Pt would be improved, which might be explained via bifunctional or ligand effect mechanisms.⁶⁻⁷ In this Chapter, we report on the electrocatalytic activity of Pt-Ir nanoparticles and investigate the effects of the substrate and the composition of nanoparticles on the oxidation of methanol. Pt-Ir nanoparticles were deposited directly onto TiO₂NTs by using chemical reduction method.⁸ Scanning electron microscopy (SEM) and energy-dispersive X-ray spectroscopy (EDX) were employed to characterize the fabricated Pt-Ir

electrocatalysts. In this study, Pt-Ir nanoparticles with different compositions were successfully deposited, and our electrochemical studies have shown that the desposition of Pt-Ir nanoparticles on the TiO₂NTs exhibited much higher activity for methanol oxidation than the Pt nanoparticles alone.

3.2 Experimental Methods

A series of Pt-Ir nanoparticles having various compositions were synthesized and directly deposited onto TiO₂NT substrates via chemical reduction method, which are described in Chapter 2. The metal precursors were prepared as follows: 0.0819 g of H₂Pt₆Cl dissolved in 2 ml of ultrapure water, and 0.0048 g of IrCl₃ dissolved in 2 ml of ultrapure water. Sodium borohydride was used as the reducing agent. The mixed Pt and Ir precursor solutions with different ratios of Pt:Ir (80:20, 70:30, 60:40, 40:60) were prepared. Aliquots (0.5M NaOH) were added to the Pt-Ir precursor solutions to stabilize the pH to between 9.5 and 10.0. The mixed solutions were then sonicated for 20 min. The following procedure was used to prepare the TiO₂NT/PtIr electrodes: each treated TiO₂NT electrode was coated with 15 µL of the mixture, followed by adding 15 µL of 1 M NaBH₄ for the chemical reduction.¹¹ The electrodes were held for 15 min and then rinsed with ultrapure water and dried at 20 ± 2°C. The aforementioned coating process was repeated to investigate the effect of the coating loads on the electrocatalytic behaviors of the formed TiO₂NT/PtIr electrodes. In addition to the Pt-Ir mixtures, a pure Pt electrode was prepared in the same fashion as the Pt-Ir electrodes, for comparison. The surface morphology of all prepared TiO₂NTs was characterized using a Hitachi SU-70 Schottky Field Emission SEM. Also, the surface composition of the 60:40 mixture was investigated and recorded via EDX with the application of 15 kV.

The electrochemical performance of all electrodes was studied using a three-electrode electrochemical system at room temperature as described in Chapter 2. The reference electrode consisted of Ag/AgCl (1M KCl) connected to the cell through a salt bridge composed of KCl, and the fabricated TiO₂NT/PtIr and TiO₂NT/Pt electrodes were used as the working electrode. A 0.5 M H₂SO₄ electrolyte was utilized to examine the hydrogen adsorption/desorption as well as the oxide formation/reduction behaviors of the electrodes, whereas the 0.1M CH₃OH +0.5 M H₂SO₄ electrolyte employed to investigate the methanol oxidation activity of the electrodes. Prior to the electrochemical measurements, ultrapure Ar gas (99.999%) was infused continuously into the electrolyte solution for 15 min. During the electrochemical experiments, Ar gas was also constantly passed above the solutions.

The electrochemical methods employed in this research included cyclic voltammetry (CV), chronoamperometry (CA), and electrochemical impedance spectroscopy (EIS). The scan rate applied for CV was 20 mV/s. CA was carried out by initially holding the potential at 0.0 mV for 30 s and then stepping to 350 mV or 650 mV for 300 s. In the EIS measurements, the electrode potential was held at 350 mV, the amplitude of modulation potentials was 10 mV, and the frequency was changed from 40kHz to 40mHz.

3.3 Pt-Ir surface analysis and composition

The surface morphology of the formed TiO₂NTs and the PtIr nanoparticles deposited on the TiO₂NTs was characterized using SEM. Figure 3.1 A reveals the formation of the well-compacted TiO₂NTs that were directly grown on the titanium substrate via the electrochemical anodic oxidation technique as described in Chapter2. These NTs possessed diameters that ranged from 90 to 120 nm, with wall thicknesses that ranged from 90 to 100 nm. As illustrated in

Figure3.1 B, PtIr nanoparticles were uniformly distributed on the TiO₂NTs with the particle size ranged from 10 to18 nm.

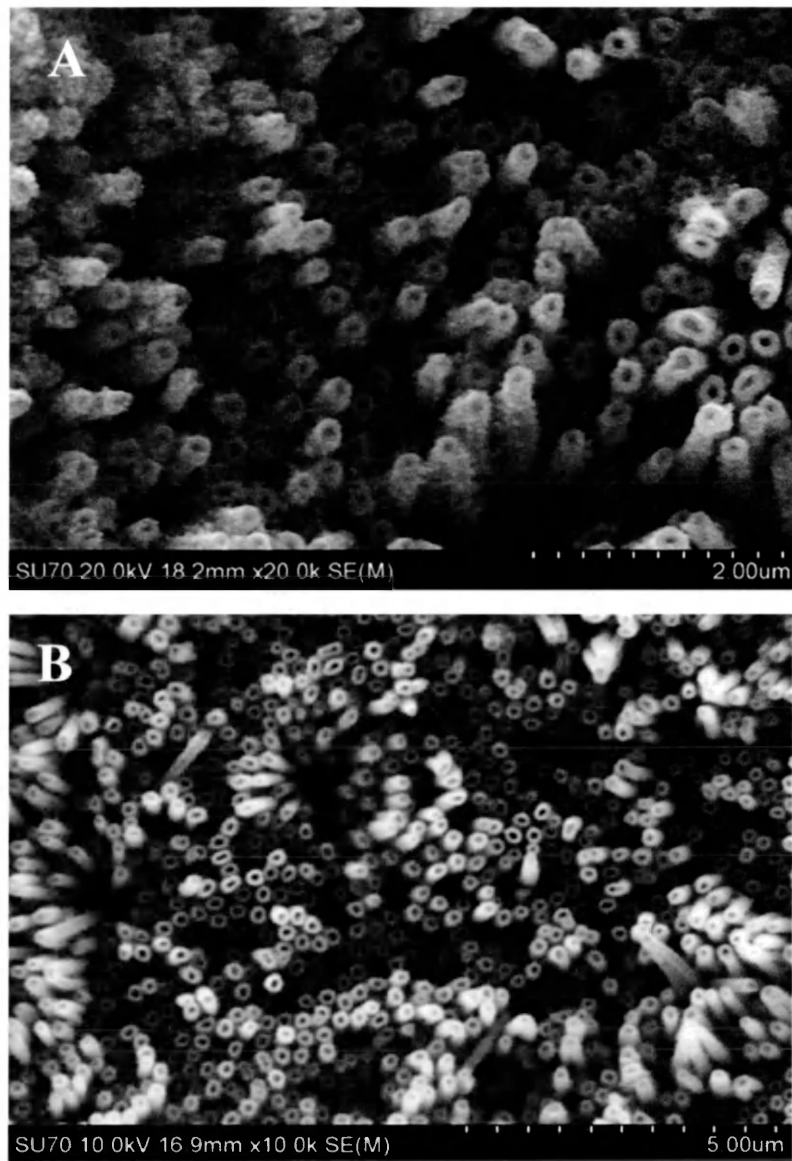


Figure 3.1 SEM images of: (A) the formed TiO₂NTs; and (B) the TiO₂NT/PtIr electrode with the Pt:Ir ratio of 60:40.

Figure 3.2A presents a typical EDX spectrum of the TiO₂NT/PtIr electrode, exhibiting strong Ti, O, Pt and Ir peaks. Quantitative analysis revealed that the ratio of Pt:Ir was very close to 60:40, which is consistent with the mixed precursor solution used for the preparation of this electrode. Figure 3.2 B – C display the EDX mapping of Pt and Ir, further confirming that the PtIr nanoparticles were uniformly deposited on the TiO₂NT electrode.

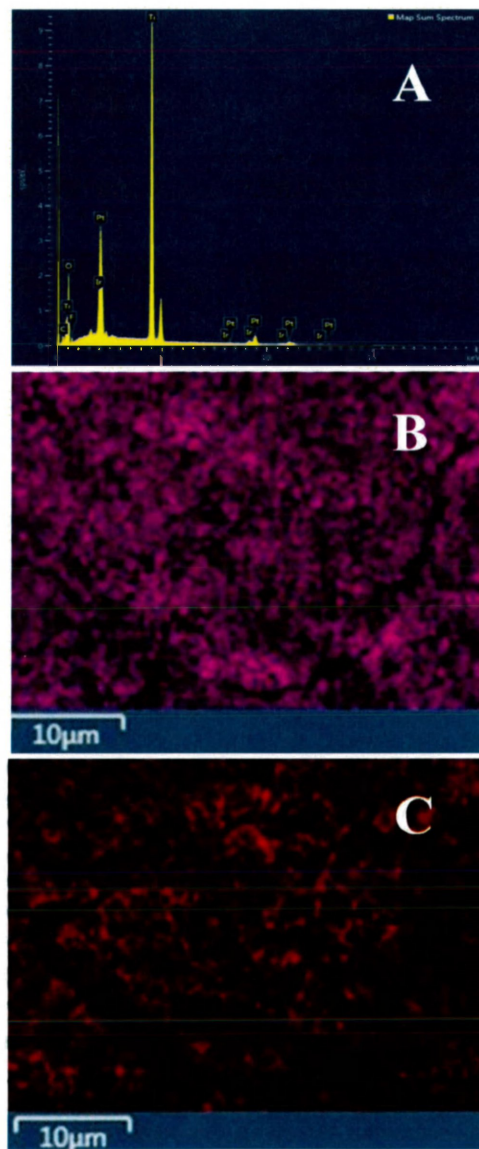


Figure 3.2 (A) EDX Spectrum of the TiO₂NT/PtIr electrode with the Pt:Ir ratio of 60:40. (B) EDX elemental mapping of Pt; and (C) EDX elemental mapping of Ir of the same TiO₂NT/PtIr electrode.

3.4 The electrochemical behaviours of the TiO₂NT/PtIr nanostructures

Cyclic voltammetry was applied to study the effects of different catalyst loads with the Pt:Ir ratio of 60:40 on the TiO₂NT electrode fabricated using the chemical reduction method as described in Chapter 2. Figures 3.3 A and B present the short potential range and long potential range CVs of the TiO₂NT/PtIr electrodes with three, six and nine depositions, respectively, recorded in a 0.5 H₂SO₄ solution at a scan rate 20 mV/s. As seen in Figure 3.3 A, the hydrogen adsorption and desorption peaks increased with the increase of the number of deposition from three coats to nine coats. The current density of the double layer was also increased, showing the increase of the electrochemical active surface area. As shown in Figure 3.3B, when the up-limit electrode potential was extended from 0.6 to 1.35V, oxide formation occurred with a broad peak centred at 0.8 V when the electrode potential was scanned from 0.6 to 1.35V; and the formed oxide was reduced with a strong peak at ~0.45V when the electrode potential was swept from 1.35 to 0.2 V.¹⁸⁻¹⁹ As the load of the Pt-Ir catalyst mixture was increased, both oxide formation and reduction peaks increased, indicating that a higher electroactive surface area was obtained by increasing the catalyst loads.

The catalytic activity of the Pt-Ir nanostructures towards the electrochemical oxidation of methanol was investigated. Figure 3.3 C presents the CVs of the TiO₂NT/PtIr electrodes recorded in 0.5 M H₂SO₄ + 0.1 M CH₃OH under a potential range between -0.225 and 1.35 V at a scan rate of 20 mV/s. As mentioned above, the sample electrodes carried different catalyst loads, with successive loads consisting of an additional 15 mg of the catalyst. Greater catalyst loads increased the oxidation peak to the maximum current density at a potential of 0.70 V. Thus, catalyst loads may play a role in terms of the electrocatalytic activity of electrodes. There is a positive relationship between increasing the catalyst load and enhancing catalytic activity.

Despite the observation that increasing the number of catalyst loads served to continually increase the electrocatalytic methanol oxidation activity, three loads were sufficient to provide the improvements necessary for the purposes of this study. Considering that these metals are quite expensive, the increases in electrocatalytic activity obtained by four or more loads may not provide attractive enough benefits to offset the cost of additionally incorporated materials.

A general electrochemical characterization of the different $\text{TiO}_2\text{NT}/\text{PtIr}$ electrodes with the different Pt:Ir ratios of 100:0, 70:30, 60:40 and 50:50, but with the same amount of the catalyst, was carried out. Figures 3.4 A and B present the short potential range and the long potential range CVs of the $\text{TiO}_2\text{NT}/\text{Pt}$ and the $\text{TiO}_2\text{NT}/\text{PtIr}$ electrodes recorded in 0.5 M H_2SO_4 at a scan rate 20 mV/s. As depicted in Figure 3.4A, the CVs in the hydrogen region with a potential ranging from -0.225 to 0.60 V vs SCE, illustrated that additional volumes of Ir served to increase the active surface area. The $\text{TiO}_2\text{NT}/\text{PtIr}$ (60:40) electrode exhibited the largest electroactive area. Similarly, Figure 3.4B illustrates that the typical hydrogen adsorption and desorption peaks as well as oxide formation and reduction peaks appeared in the potential range from -0.225 to 1.350 V vs SCE. The reduction peaks, which were distinguished at 1.20 V, confirmed the presence of Ir. Additionally, the peaks at 0.40 V for the mixed Pt-Ir electrodes verified the existence of Pt, where the Pt-Ir electrodes had a lower potential in comparison to the pure Pt electrodes. While the reduction current of the formed Ir oxide was decreased, the reduction current of the formed Pt oxide was elevated as the Pt volume increased. The impact of increasing the volume of Ir within the nanoparticles on both the reduction current density and oxidation peaks at 0.40 V and 1.20V, confirming the existence of Ir in alloys.

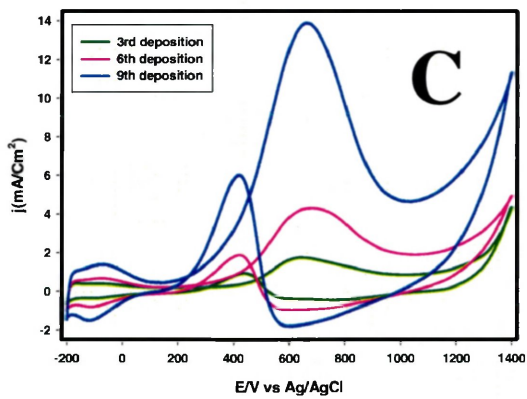
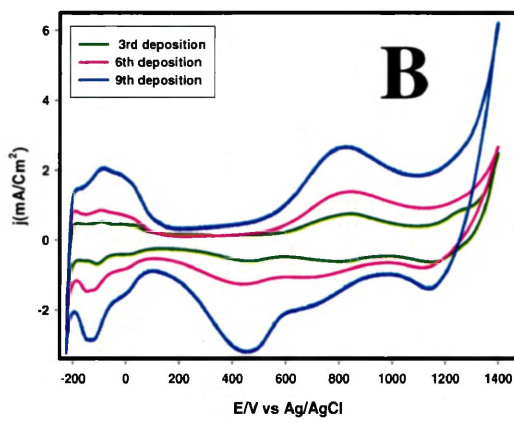
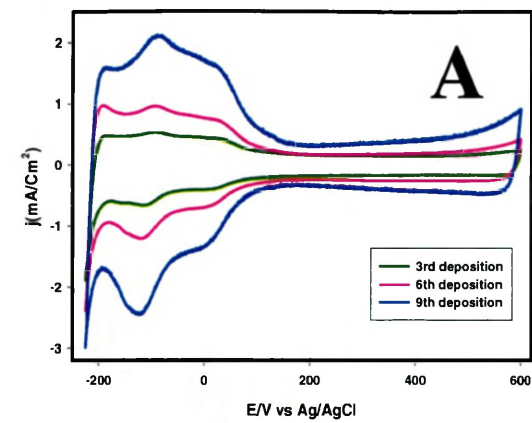


Figure 3.3 (A) Cyclic voltammograms of the effect of different loadings of PtIr on TiO_2 in $0.5\text{M}\text{H}_2\text{SO}_4$, under a scan rate of 20mVs^{-1} in different potential ranges; short (A) and long (B), the CVs methanol oxidation of different PtIr loads on TiO_2 in 0.5M of $\text{H}_2\text{SO}_4 + 0.1\text{M} \text{CH}_3\text{OH}$ under a scan rate of 20mV/s (C) .

The catalytic activities of the TiO₂NT/Pt and TiO₂NT/PtIr electrodes towards the electrochemical oxidation of methanol were further investigated. Figure 3.4C displays the CVs recorded at a scan rate of 20 mV/s in a 0.1 M CH₃OH + 0.5 M H₂SO₄ solution. Methanol oxidation via Pt electrodes may easily produce CO with other species that block Pt surface resident sites, and suppress the oxidation of methanol at potentials of lower than 0.4 V.¹⁴⁻²¹ As seen in Figure 3.4C, the onset potential for methanol oxidation was decreased from 0.4 to 0.2 V, indicating that the addition of Ir greatly promoted the electrochemical oxidation of CO along with other chemisorbed species.

Moreover, the current intensity of the peak centered at ~0.65 was significantly increased with the increase of Ir from 0.0% to 40%. However, further increase of the Ir from 40% to 50% resulted in the decrease of the peak current, showing that 60% Pt and 40% Ir was the optimum composition.

We further investigated the electrochemical activity and stability of the TiO₂NT/Pt and TiO₂NT/PtIr electrodes using chronoamperometry. Figures 3.5 A and B present the chronoamperometric curves measured at 0.35 and 0.65 V, respectively. There was a sharp initial current drop in all curves of the samples followed by a slow decay. This slow decay might be attributed to the poisoning and structural changes of the Pt-Ir nanoparticles, which are the result of potential perturbation during the reaction resulting from the presence of the intermediate produced during the oxidation of methanol as well as mass transfer. It was apparent that the steady-state current density of the TiO₂NT/PtIr(60:40) at both 0.35 and 0.60 V over the periods of 300s attained 5 mA/cm² and 45 mA/cm², respectively.

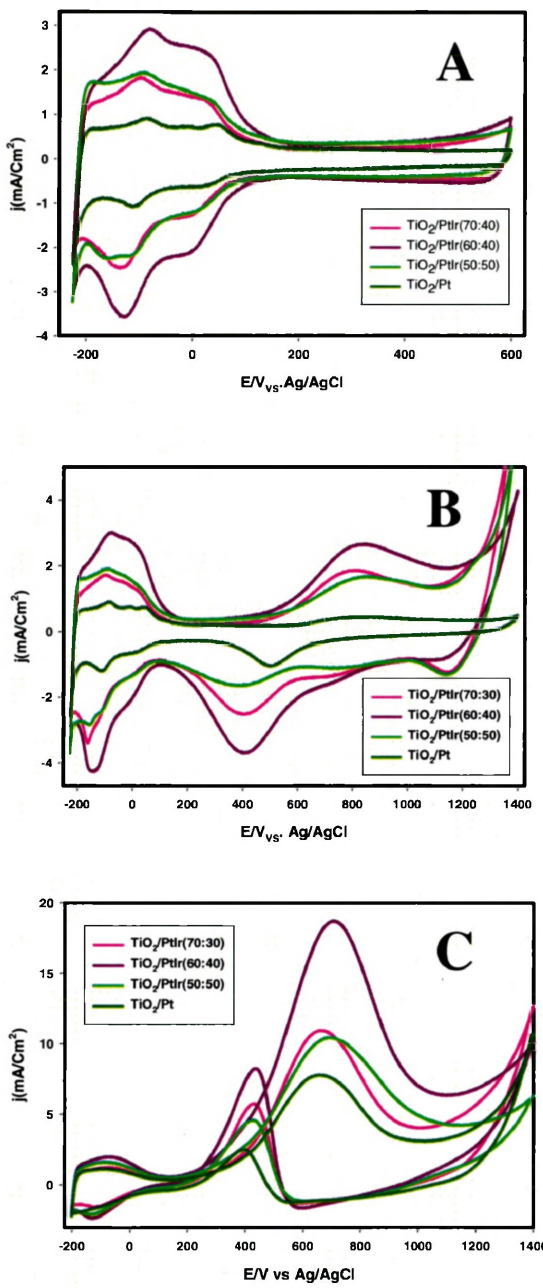


Figure 3.4 (A) Cyclic voltammograms of the effect of different PtIr compositions on TiO_2 in $0.5\text{M}\text{H}_2\text{SO}_4$, under a scan rate of 20mVs^{-1} in different potential ranges; short (A) and long (B), the CVs of methanol oxidation of different PtIr compositions on TiO_2 in 0.5M of $\text{H}_2\text{SO}_4 + 0.1\text{M}$ CH_3OH , under a scan rate of 20mV/s (C)

These values significantly exceeded the current density of the TiO₂NT/Pt electrode, which was 3 mA/cm² at 0.35 and 0 mA/cm² at 0.65 V, indicating the high tolerance of Pt-Ir electrodes to CO-like intermediates, and a high catalytic stability.¹⁴⁻²² The above results show that adding a specific composition of Ir to Pt may induce a significant enhancement of the performance of catalysts .

Electrochemical impedance spectroscopy was employed to examine the charge transfer electrochemical reaction resistance of methanol oxidation. Figure 3.8 presents three Nyquist plots of the TiO₂NT/Pt and the TiO₂NT/PtIr electrodes recorded at the electrode potential of 0.35 V in a 0.1 M CH₃OH + 0.5 M H₂SO₄ solution, where Z_r and Z_i represented the real and imaginary impedance components. The equivalent circuit shown in the inset was used to fit the experimental data. R_s represents the uncompensated solution resistance, whereas R_p symbolizes the polarization resistance. The capacitor defined as C, which is the double-layer capacitance. Table 1 displays the corresponding data for all the elements. It was noticeable that R_s was in the range of ca.0.872 - 1.057 Ω cm² at different potentials due to the same supporting electrolyte. The small errors indicated that the proposed electrical model effectively fitted the EIS data. The TiO₂NT/PtIr(60:40) exhibited the lowest charge transfer resistance at about 11.88 Ωcm², which was lower than 18.75 Ω cm² for Pt. These results are consistent with the aforementioned CV and CA measurements, further demonstrating that the TiO₂NT/PtIr(60:40) possessed the optimum composition and exhibiting the highest electrocatalytic activity.

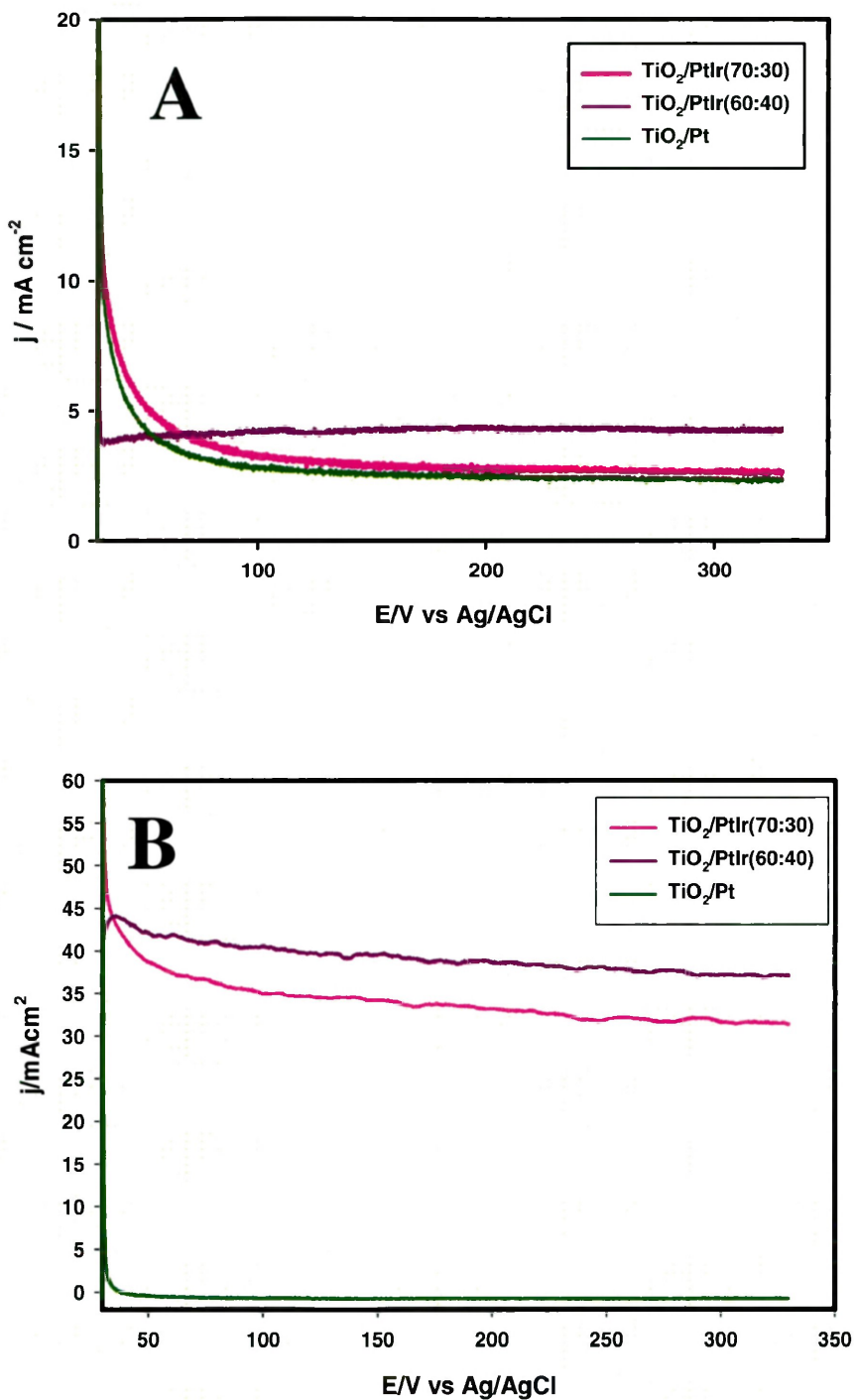


Figure 3.5 Chronoamperometric curves of CH_3OH electrooxidation on TiO_2/PtIr catalysts in 0.1 M $\text{CH}_3\text{OH} + 0.5 \text{ M H}_2\text{SO}_4$ at a potential of 350mV, and 650mV vs SCE shown in parts (A) and (B) in 0.1 M $\text{CH}_3\text{OH} + 0.5 \text{ M H}_2\text{SO}_4$

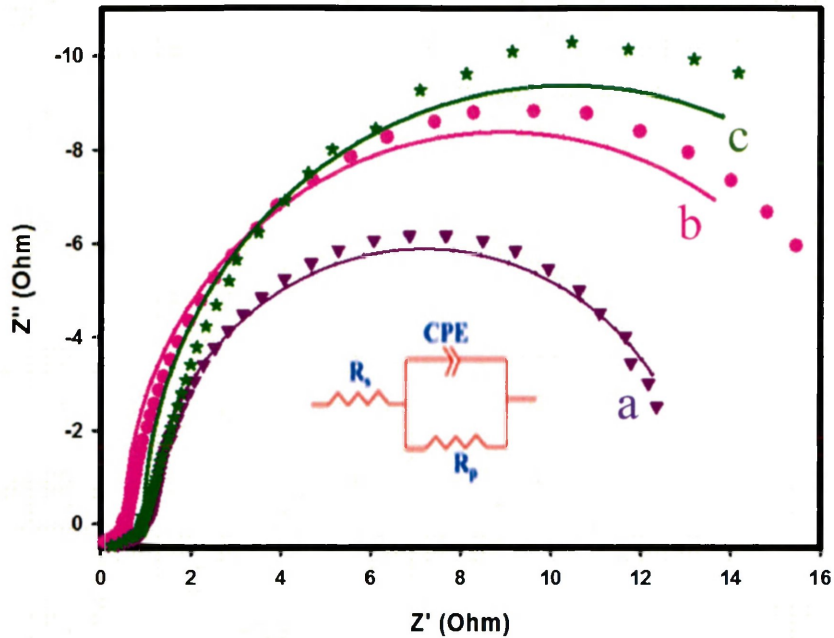


Figure 3.6 Nyquist plots of the TiO₂NT/Pt, and TiO₂NT/PtIr electrodes with Pt:Ir 70:30, 60:40 compositions in the nanocomposites on the TiO₂NT electrodes recorded in 0.5M H₂SO₄ + 0.1 M CH₃OH. The frequency was altered, from 100 kHz to 40 mHz, with an applied potential of 0.350V and Inset: The corresponding equivalent electric circuit.

3.5 Conclusions

PtIr nanoparticles with different compositions were successfully deposited onto TiO₂NTs using a facile sodium borohydride reduction method at room temperature. The TiO₂NTs were directly grown on the Ti substrate using an electrochemical anodization method. The catalytic activity of the Pt-Ir nanoparticles depends, to a significant degree, on their composition. The successful reduction of a Pt-Ir noble metal load was achieved at an optimal percentage of 60% Pt and 40% Ir, exhibiting an increased current density for the oxidation of methanol. In the EIS study, the TiO₂NTs/PtIr(60:40) electrode demonstrated the lowest charge transfer resistance and highest electrocatalytic activity for the oxidation of methanol, promising for the DMFC applications.

Table.3.1 Values of elements in an equivalent electric circuit fitted in the Nyquist plots of Figure.3.8

Electrodes	Rs ($\Omega \text{ cm}^2$)		R_p ($\Omega \text{ cm}^2$)		Capacitance (C) (mF.cm^{-2})	
	Value	Error (%)	Value	Error (%)	Value	Error (%)
TiO ₂ /PtIr(60:40)	1.057	0.596	11.88	1.743	0.025	1.18
TiO ₂ /PtIr(70:30)	0.544	0.969	16.77	0.484	0.022	1.458
TiO ₂ / Pt	0.872	0.849	18.75	3.004	0.023	1.451

References

- (1) Chen, A.; Matyasovszky, N.; Tian, M.; MacDonald, D. “Advanced approaches to lignin modification”, in “Lignin Properties and Applications in Biotechnology and Bioenergy”, R. J. Paterson (ed.), Nova Science Publishers, Inc., **2012**, Chapter 10, Pages 331 – 354.
- (2) Tolba, R.; Tian, M.; Wen, J.; Jiang, Z.-H.; Chen, A. *J. Electroanal. Chem.* **2010**, *649*, 9.
- (3) Chen, A.; J, D.; Russa, L.; Miller, B. *Langmuir*. **2004**, *20*, 9695.
- (4) Tian, M.; Wen, J.; MacDonald, D.; Asmussen, R.M.; Chen, A. *Electrochim. Commun.* **2010**, *12*, 527.
- (5) Li, X.; Clarke, K.; Li, K.; Chen, A. *Biotechnol. Progress*. **2012**, *28*, 1389.

- (6) Tremiliosi-Filho, G.; Kim, H.; Chrzanowski, W.; Wieckowski, A.; Grzybowska, B.; Kulesza, P. *J. Electroanal. Chem.* **1999**, *467*, 143.
- (7) Pan, K.; Tian, M.; Jiang, Z.-H.; Kjartanson, B.; Chen, A. *Electrochim. Acta.* **2012**, *60*, 147.
- (8) Tian, M.; Thind, S.S.; Chen, S.; Matyasovszky, N.; Chen, A. *Electrochim Commun.* **2011**, *13*, 1186.
- (9) Tian, M.; Malig, M., Chen, S. and Chen, A., *Electrochim. Commun.*, **2011**, *13*, 370.
- (10) Chen, S.; Malig, M.; Tian, M.; Chen, A. *J. Phys. Chem. C.* **2012**, *116*, 3298.
- (11) Glavee, G.N.; Klabunde, K. J.; Sorensen, C. M.; Hadjapanayis, G. C. *Langmuir.* **1992**, *8*, 771.
- (12) Zhang, S.; Shao, Y. Y.; Yin, G. P.; Lin, Y. H. *J. Power Sources*, **2010**, *195*, 1103
- (13) Xing, L.; Jia, J.; Wang, Y.; Zhang, B.; Dong, S. *Int.J. Hydrogen energy*, **2010**, *35*, 12169.
- (14) Ocampo, A.L.; Jiang, Q-Z.; Ma, Z-F.; Varela, J.R.; Gyves, J.D. *Electrocatalysis*, **2014**, *5*, 387.
- (15) Grigorjeva, A.V.; Goodilin, E. A.; Derlyukova, L.E.; Anufrieva, T.A.; Tarasov, A.B.; Dobrovolskii, Y.A.; Tretyakov, Y.D. *Applied Catalysis A: General*, **2009**, *362*, 20.
- (16) Watanabe, M.; Motoo, S. *J. Electroanal. Chem.* **1975**, *60*, 275.
- (17) Gasteiger, H. A.; Markovic, N.; Ross Jr, P.N.; Cairns, E. J. *J. Electrochem. Soc.* **1994**, *141*, 1795.
- (18) MacDonald, J.P.; Gualtieri, B.; Runga, N.; Teliz, E.; Zinola, C.F. *Int.J. Hydrogen energy*, **2008**, *33*, 7048.

- (19) X.H, Xia. *Electrochim Acta*, **1999**, *45*(7), 1057.
- (20) Waszczuk, P.; Solla-Gull, J.; Kim, H-S.; Tong, Y.Y.; Montiel, V.; Aldaz, A.; Wieckowski, A. *J. Catalysis*, **2001**, *203*, 1.
- (21) Shen, L.; Jiang, Q-Z.; Gan, T.; Shen, M.; Rodriguez Varela, FJ.; Ocampo, A.L.; Ma, Z-F. *J. New Mater. Electrochem. Syst*, **2010**, *13*, 205.
- (22) Jiang, Q-Z.; Wu, X.; Shen, M.; Ma, Z-F.; Zhu, X-Y. *Catal. Lett*, **2008**, *124*, 434.

Chapter 4 Synthesis and electrochemical study of Pt-Ru nanoparticles deposited on TiO₂NTs for methanol oxidation

4.1 Introduction

To date, the most commonly utilized catalytic electrodes in fuel cells incorporate Pt. For example, in DMFCs, anodes are comprised of either platinum or platinum-based electrode materials. As methanol oxidation occurs at the anode surface, Pt is employed in DMFC due to its attractive activity in methanol activation, namely the cleaving of C–H bonds, which leads to the formation of carbon monoxide (CO) at the anode surface.¹ Unfortunately, the formed CO poisons the electrode, thereby reducing its efficiency. Hence, in order to improve the electrode and avoid the deleterious poisoning of platinum, the CO should be removed from the surface via oxidation to CO₂.¹ Since the oxidation of CO via a pure Pt catalyst is slow, the addition of transition metals (e.g., Ir, Sn, W, Mo, Ru) to the electrode may serve to decrease the presence of CO, due to the desirable activity of transition metals in promoting the oxidation CO to CO₂.^{1,2} Ruthenium (Ru) is such a transition metal that may enhance the catalyst by promoting the activation of water and to facilitate the concomitant transfer of oxygen to CO as it transforms to CO₂.^{3,4} This enhancement can be explained through a bifunctional and ligand mechanism.⁵ In this chapter, the potential of Ru to augment the performance of DMFC was tested using TiO₂ nanotubes (TiO₂NTs) as the supporting electrodes. TiO₂ was employed due to its high stability, chemical inertness, low cost, and non-toxic properties.⁶⁻⁹ Additionally, the electrocatalytic activity of PtRu nanoparticles was investigated, as were the effects of the substrate and nanoparticle compositions on the oxidation of methanol.

In this work, Pt-Ru nanoparticles with different compositions were deposited on TiO₂NTs using a chemical reduction method. The fabricated TiO₂NT/Pt-Ru electrocatalysts were

characterized with SEM, EDX and electrochemical techniques. Our studies have shown that the TiO₂NT/Pt-Ru nanoaprticles exhibited more robust activity for methanol oxidation in comparison to Pt nanoparticles deposited on the TiO₂NTs.

4.2 Experimental and Methods

A set of Pt-Ru nanoparticles having various compositions were synthesized and directly deposited onto TiO₂NT substrates using a chemical reduction method, where sodium borohydride was employed as the reducing agent. For the chemical reduction method, metal precursors were prepared as follows: 0.0819 g of H₂PtCl₆ was dissolved in 2 mL of ultrapure water, and 0.0414 g of RuCl₃ was dissolved in 2 mL of ultrapure water. The desired compositions of Pt-Ru (70:30, 60:40, 50:50) were obtained by mixing the appropriate Pt and Ru precursors. Aliquots (0.5M NaOH) were added to the mixed Pt and Ru precursor solutions to stabilize the pH to between 9.5 and 10. The solutions were then sonicated for 20 min. The following procedure was used to prepare the TiO₂NT/PtRu electrodes: each treated TiO₂NT electrode was coated with 15 µL of the mixture, followed by adding 15 µL of 1 M NaBH₄ for the chemical reduction.⁷ The electrodes were held for 15 min and then rinsed with ultrapure water and dried at 20 ± 2°C. The aforementioned coating process was repeated to investigate the for comparison between different ratio of the metal on the electrocatalytic behaviors of the formed TiO₂NT/PtRu electrodes. The surface morphology of all prepared TiO₂NTs was characterized using a Hitachi SU-70 Schott Field Emission SEM. Also, the surface composition of the 60:40 mixture was investigated and recorded via EDX with the application of 15 kV.

The electrochemical performance of all electrodes was accomplished using a three-electrode electrochemical system at the room temperature as described in Chapter 2. The reference electrode consisted of Ag/AgCl (1M KCl) connected to the cell through a salt bridge

composed of KCl, and the fabricated TiO₂NT/PtRu and TiO₂NT/Pt electrodes were used as the working electrode. A 0.5 M H₂SO₄ electrolyte was utilized to examine the hydrogen adsorption/desorption as well as the oxide formation/reduction behaviors of the electrodes, whereas the 0.1M CH₃OH +0.5 M H₂SO₄ electrolyte was employed to investigate the methanol oxidation activity of the electrodes. Prior to the electrochemical measurements, ultrapure Ar gas (99.999%) was infused continuously into the electrolyte solution for 15 min. During the electrochemical experiments, Ar gas was also constantly passed above the solutions.

The electrochemical methods employed in this work included cyclic voltammetry (CV), and chronoamperometry (CA). The scan rate applied for CV was 20 mV/s. CA was carried out by initially holding the potential at 0.0 mV for 30 s and then stepping to 600 mV or 650 mV for 300 s.

4.3 Pt-Ru surface analysis and composition

Scanning electron microscopy was used to characterize the surface morphology of the fabricated catalyst dispersed onto the TiO₂NT samples. Figure 4.1 A reveals the formation of the well-compacted TiO₂NTs that were directly grown on the titanium substrate via the electrochemical anodic oxidation technique as described in Chapter2. Figure 4.1B shows the formed NTs with diameters that ranged from 90 to 120 nm, with wall thicknesses that ranged from 90 to 100 nm. As shown in Figure 4.1 C and D, the nanoparticles with a diameters that ranged from 8nm to 15nm were uniformly deposited onto the TiO₂NT support.

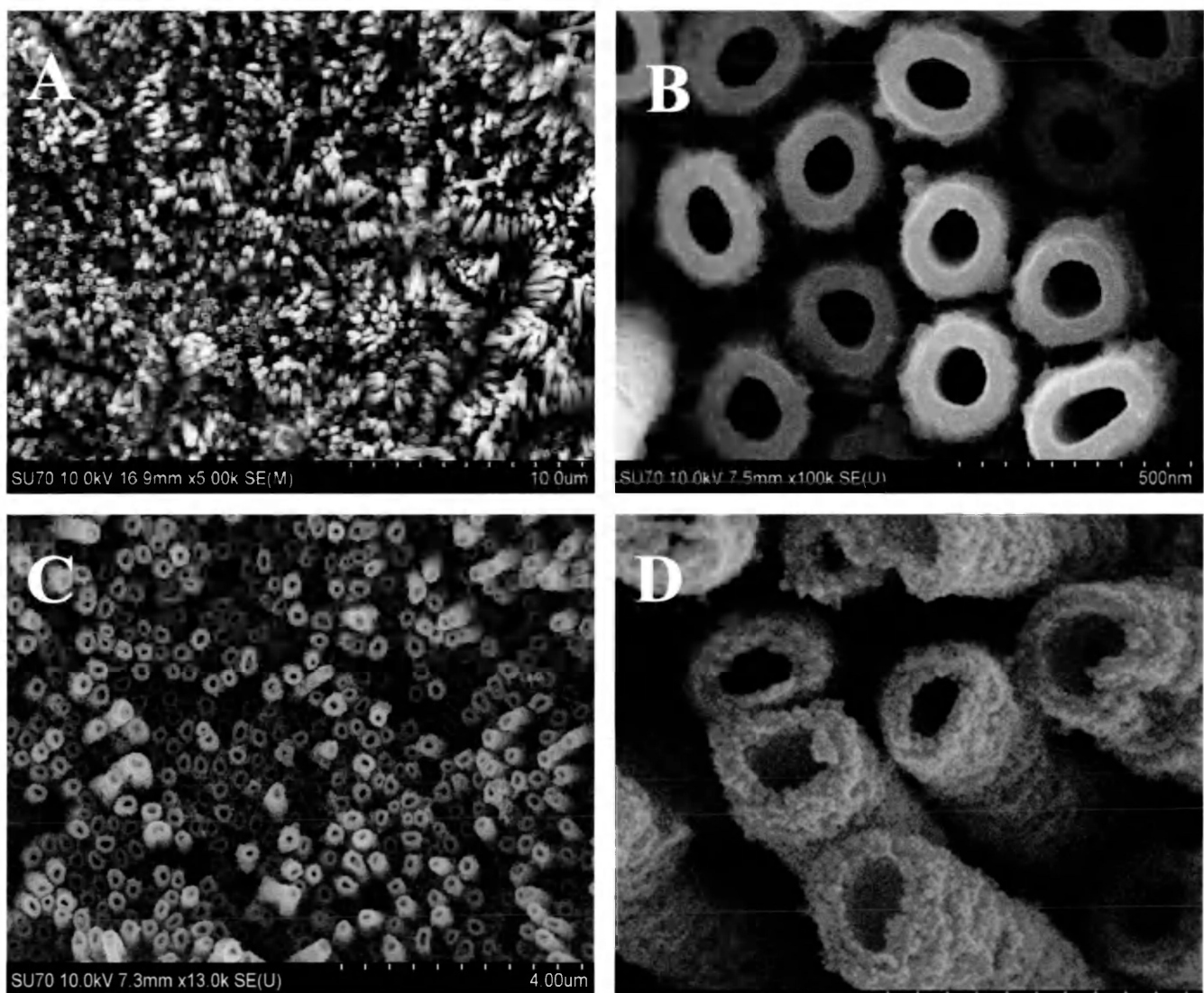


Figure 4. 1 SEM images of the TiO₂NTs (A), the TiO₂NT electrode under high magnification (B), TiO₂NT/PtRu nanoparticles under low-magnification (C), the PtRu nanoparticles on the TiO₂NT (D).

Figure 4.2A presents a typical EDX spectrum of the TiO₂NT/PtRu electrode, exhibiting strong Ti, O, Pt and Ru peaks. Quantitative analysis revealed that the ratio of Pt:Ru was very close to 60:40, which is consistent with the mixed precursor solution used for the preparation of this electrode. Figure 4.2 B – D display the EDX mapping of Ti, Pt and Ru, respectively, further confirming that the PtRu nanoparticles were uniformly deposited on the TiO₂NT electrode.

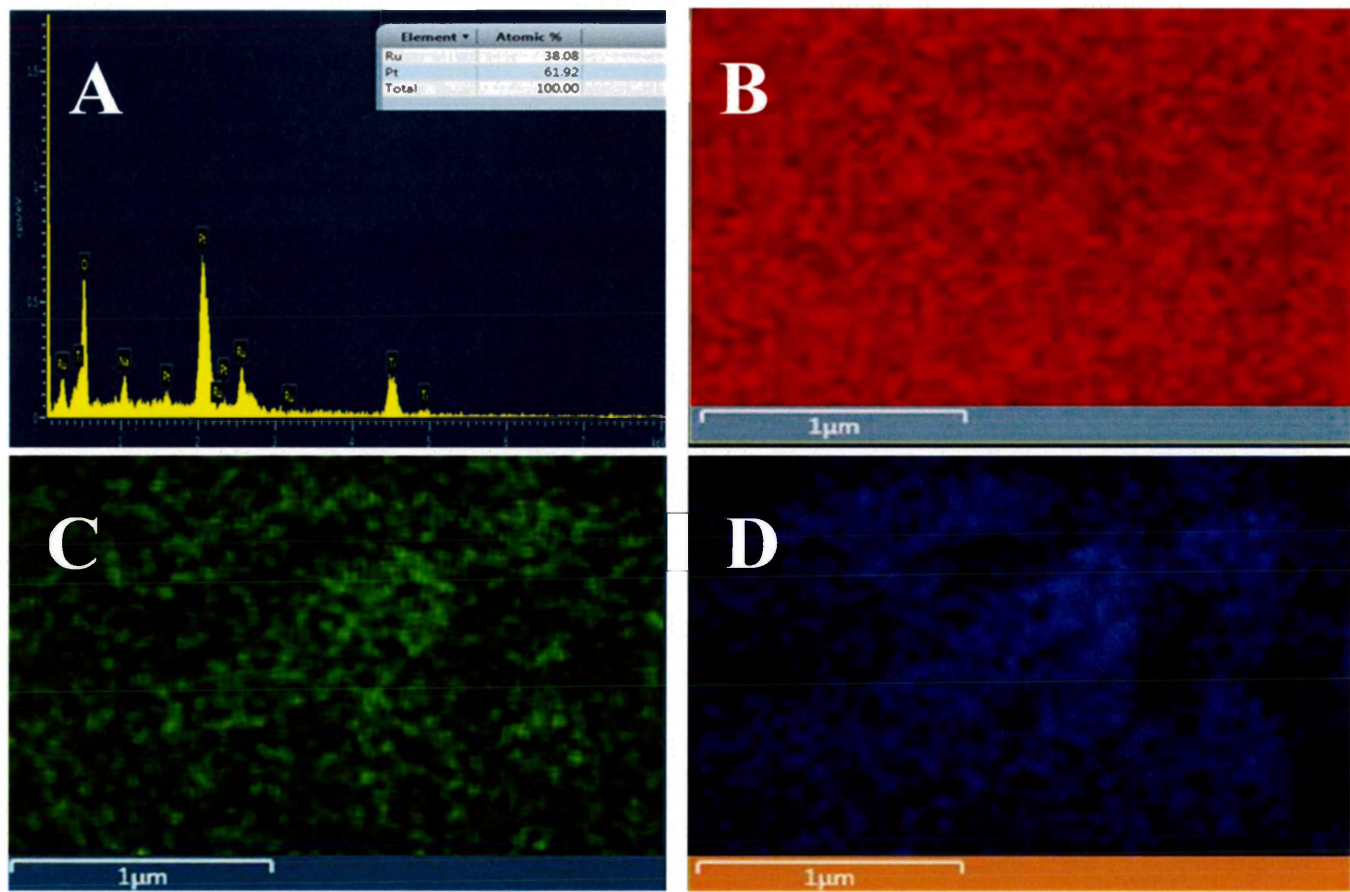


Figure 4.2 (A) EDS of the PtRu/TiO₂NT electrodes with the PtRu/TiO₂NT 60:40 composition, Elemental mapping of the Ti (B), Pt (C) and Ru (D) obtained at the Pt-Ru 60:40 electrode.

4.4 Electrochemical behaviour of the TiO₂NT/PtRu nanostructures

The electrochemical characterization of the fabricated TiO₂NT/PtRu electrodes with the different Pt:Ru ratios of 100:0, 70:30, 60:40 and 50:50, but with the same amount of the catalyst, was carried out. Figure 4.3 presents the CVs of the TiO₂NT/Pt and the TiO₂NT/PtRu electrodes recorded in a 0.5 M H₂SO₄ solution in the electrode potential range from -0.225 to 1.250 V at a scan rate of 20 mV/s. As depicted in Figure 4. 3, the CVs in the hydrogen region with a potential ranging from -0.225 V to 100 mV vs SCE, illustrated that additional volumes of Ru served to increase the hydrogen adsorption and desorption as well as the electrochemical active surface area. The TiO₂NT/PtRu(60:40) electrode exhibited the largest electroactive area. Oxide formation and reduction were observed in the electrode potential range from 0.150 to 1.250 V. The addition of Ru resulted in a negative shift of the onset potential of the oxide formation. The strong reduction peak, which was distinguished at ~0.400 V, confirmed the presence of Ru. Additionally, the peaks at 0.400 V for the mixed Pt-Ru electrodes verified the existence of Pt, where the Pt-Ru electrodes had a lower potential in comparison to the pure Pt electrodes.

4.5 Electrooxidation of methanol oxidation on the TiO₂NT/Pt and TiO₂NT/PtRu nanostructures

Figure 4.4 presents the CVs of the various TiO₂NT/Pt and TiO₂NT/PtRu (100:00, 70:30, 60:40, 50:50) electrodes recorded in a solution of 0.1 M CH₃OH and 0.5 M H₂SO₄ at a scan rate 20mV/s in the potential ranged from -0.200 to 1.250 mV vs SCE. It was noted that the peak at 0.500 V in the forward scan was reflective of methanol electrooxidation at the TiO₂NT/PtRu (60:40) electrode the oxidation peak for the TiO₂NT/PtRu(70:30) and TiO₂NT/PtRu(60:40) electrodes was doubled and transitioned to a lower potential, in comparison to the TiO₂NT/Pt electrode.

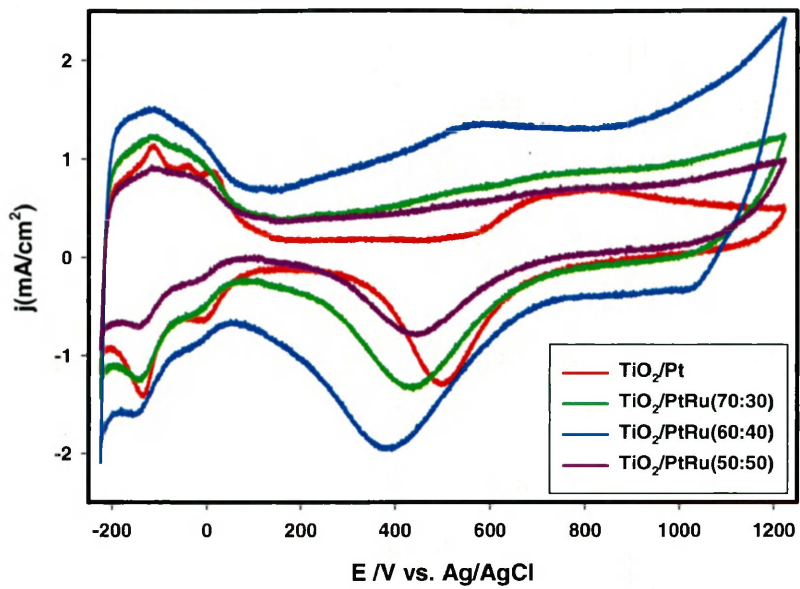


Figure 4.3 Cyclic voltammograms of the effects of different ratio of Pt-Ru on TiO_2 NTs in 0.5M H_2SO_4 at a scan rate of 20mVs⁻¹ and potential of -0.225V to 1.200V

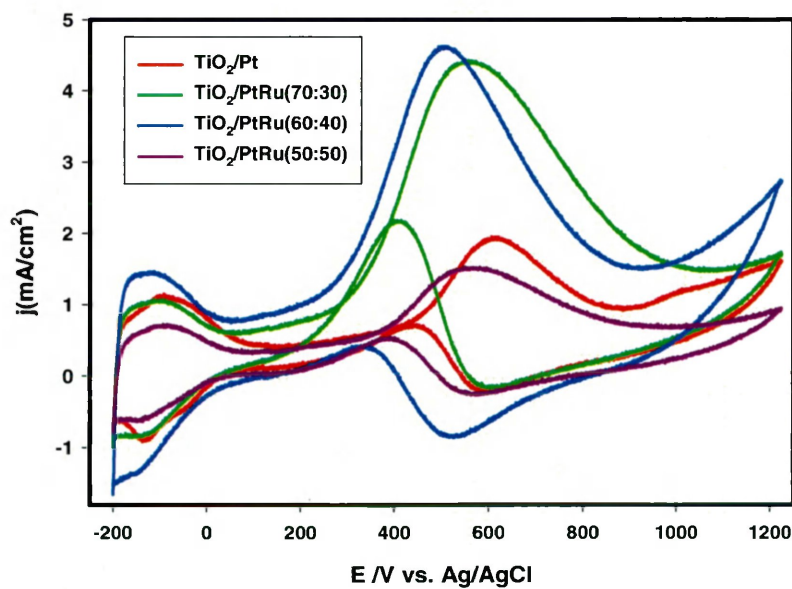
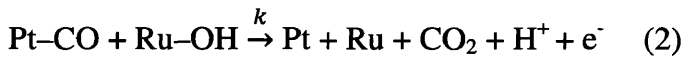
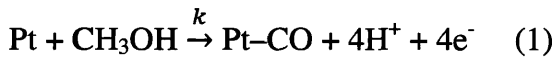


Figure 4.4 Cyclic voltammograms of methanol oxidation of different Pt-Ru ratio on TiO_2 in 0.5M of H_2SO_4 + 0.1M CH_3OH at a scan rate of 20mV/s.

The reason behind the enhancing feature of Ru on the TiO₂NT/PtRu electrode may be explained by its methanol oxidation mechanism. It is recognized that steady-state methanol oxidation includes CO on the Pt phase of the catalyst in the reaction.¹² CO must be oxidatively removed from the surface in order to release the surface sites required to sustain the reaction, which remains the steady-state current, or the continuous catalytic oxidation process.¹³ The oxidation process at the TiO₂NT/Pt electrode indicated in Fig. 4.4 was relatively slow. It can be noticed that the addition of Ru to the Pt catalyst enhances CO removal from the surface, since Ru promotes CO oxidation to CO₂ via a bifunctional mechanism.^{1,14,15}



where the OH symbolizes the oxygen-containing species, and *k* is the reaction rate constant. Although the ligand effects were realized, they were less evident than the bifunctional effects due to the dissociative character of the decomposition of methanol.¹⁶ There is the requirement for an ensemble, which comprises a specific number of Pt sites where methanol decomposes into fragments.^{1,16} In this study, as the surface consisted of Pt-Ru supported by TiO₂NTs, disregarding the Ru oxides that were possibly present on the surface, there was an ample surface density of large Pt aggregates to sufficiently decompose the methanol. In the 60:40 ratio it was likely that only Pt-Ru pairs were present on the surface. The static/dynamic distribution of Pt-Ru nanoparticle sizes allowed for the greater availability of reaction sites.¹⁷ To secure the most effective CO removal pathway associated with the relative composition of PtRu, there was a requirement to maximize the Pt sites for reaction 1 and the Ru edge site population for reaction 2. Increasing the Pt:Ru ratio above 60:40 caused a reduction in the efficiency of the steady-state methanol oxidant, confirming the importance of the relative compositions of Pt-Ru.

Since CO is the principal poisoning species involved in the oxidation of methanol over Pt catalysts, an optimized catalyst should exhibit a high catalytic activity toward the oxidation of CO.¹⁸ The catalytic activities of CO oxidation of the prepared Pt-based catalysts, TiO₂NT/Pt and TiO₂NT/PtRu (70:30, 60:40, 50:50) electrodes, are shown in Figure 4.5. For CO adsorption on the TiO₂NT/Pt and TiO₂NT/PtRu electrodes, a 0.5M H₂SO₄ solution was purged with CO for six minutes and followed by Ar purging for four minutes, while the electrode potential was held at -0.100 V. The electrode potential was scanned in the range from -0.225 to 0.900 V vs SCE at a scan rate of 10mV/s.

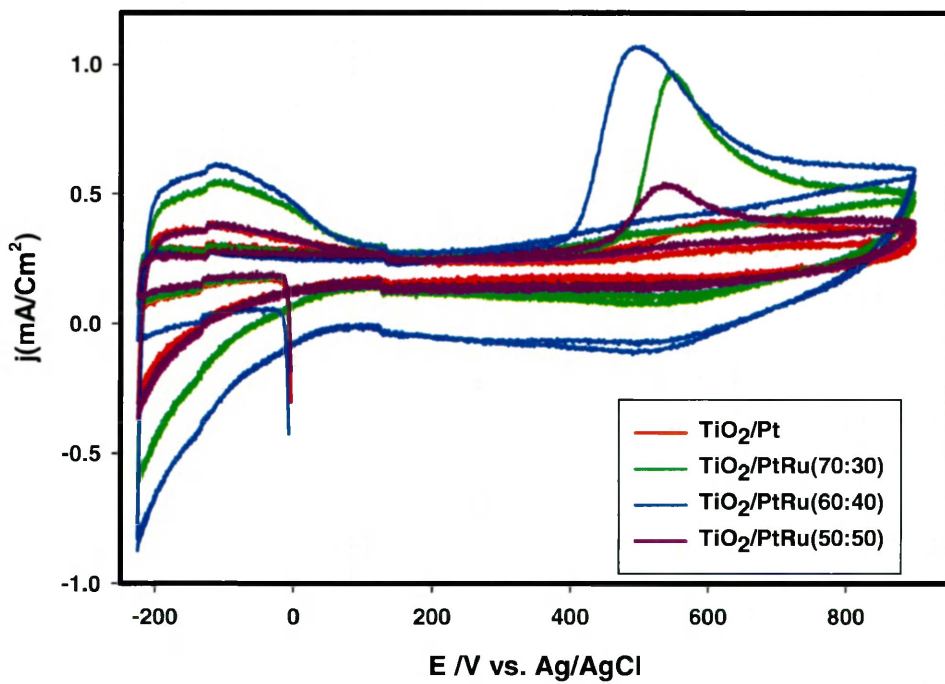


Figure 4.5 Cyclic voltammograms of CO oxidation of different Pt-Ru ratio on TiO₂ NTs in 0.5M H₂SO₄ at a scan rate of 20 mV/s.

The catalysts produced a broad peak during the first scanning cycle as a result of the oxidation of previously adsorbed CO at the electrode; whereas in the second cycle, the peak disappeared, indicating that CO was completely oxidized during the first potential scan.^{19,20} The addition of Ru significantly lower the electrode potential for the CO oxidization, thus greatly improving the catalytic activity towards methanol oxidation. The TiO₂NT/PtRu (60:40) electrode demonstrated the highest current density as well as the lowest onset potential and peak potential for CO oxidation, further confirming the beneficial effect of the addition of Ru towards the CO and methanol oxidation.²¹⁻²⁴

Chronoamperometry was utilized to investigate the activity and stability of the electrodes. The potential was held at 0.600 (Figure 4.6A) and 0.650 V (Figure 4.6B) for 300 s. In all curves of the samples, there were sharp initial current drops followed by sluggish decays. These slow decays might be attributed to PtRu nanoparticle poisoning and structural changes, which were the result of potential perturbations during the reaction, arising from the presence of intermediates generated during the oxidation of methanol.^{9,23} The current density of the TiO₂NT/PtRu (60:40) electrode at both potentials (i.e., 0.600 and 0.650 V) during the 300 s holding time attained 3.5 and 2.2 mA/cm², which was much greater than 0.7 and 0.4 mA/cm² of the TiO₂NT/Pt electrode under the same conditions. This indicated that the PtRu/TiO₂NT electrodes had a high tolerance to CO-like intermediates and a robust catalytic stability. Therefore, the addition of particular compositions of Ru to Pt might promote the enhancement of the catalyst performance.

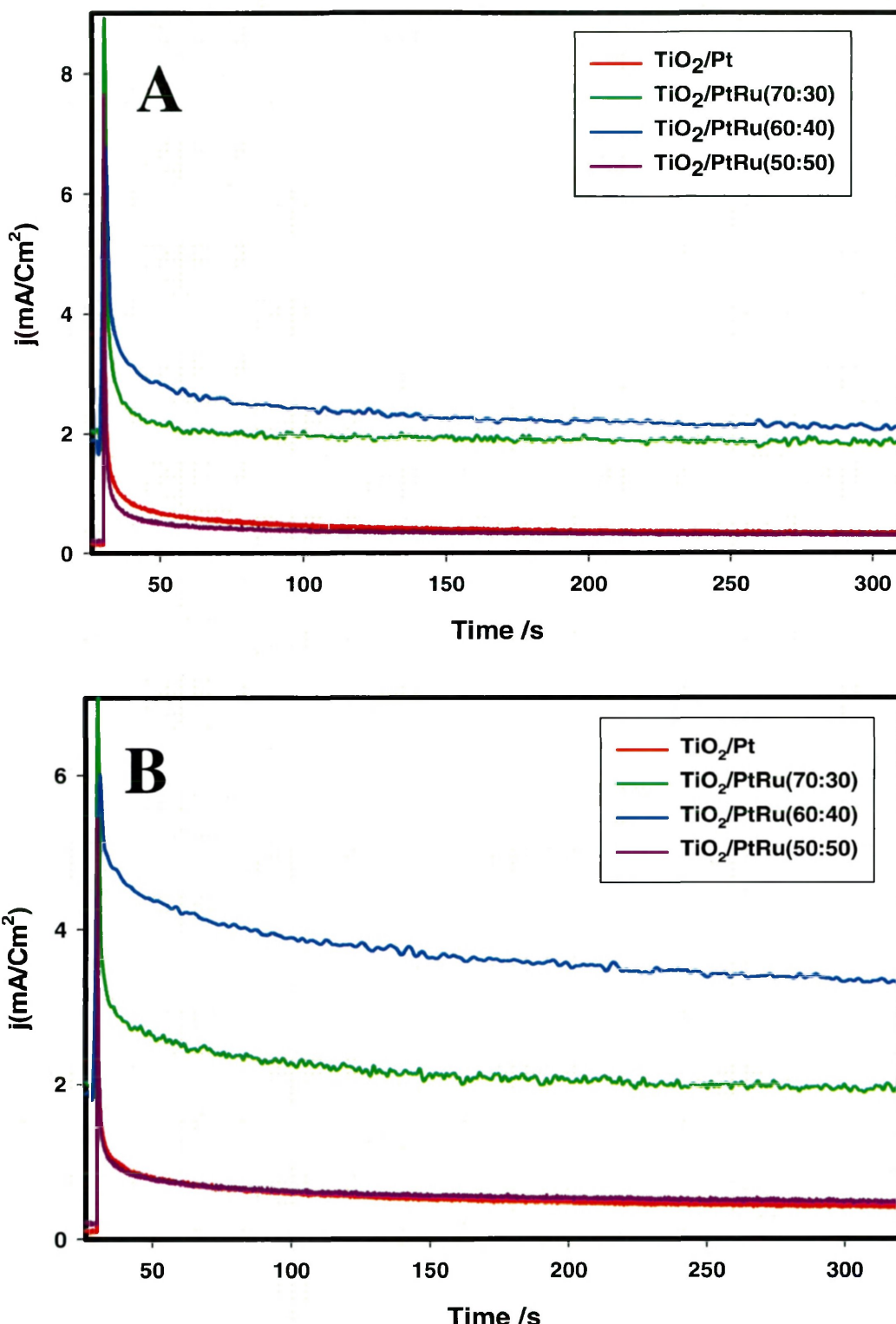


Figure 4.6 Chronoamperometric curves of CH_3OH electrooxidation on the $\text{TiO}_2\text{NT}/\text{PtRu}$ catalysts in $0.1 \text{ M } \text{CH}_3\text{OH} + 0.5 \text{ M } \text{H}_2\text{SO}_4$ at a potential of both 0.600V and 0.650V .

4.6 Conclusions

In summary, the Pt-Ru nanoparticles were uniformly dispersed onto the surface of TiO₂ nanotubes using a facile sodium borohydride reduction method at room temperature. This method effectively mediated the compositions of the formed Pt-Ru catalysts on the electrodes. In comparison to the TiO₂NT/Pt the enhancement of the oxidation of methanol was demonstrated by incorporating Ru. Further, the catalytic activity of the Pt-Ru nanoparticles was strongly dependant on their composition. The optimized composition of the Pt-Ru nanoparticles was determined to be 60% Pt and 40% Ru with the highest catalytic activity towards methanol oxidation. The TiO₂NT/PtRu (60:40) electrode demonstrated the highest current during chronoamperometry stability tests.

References

- (1) Waszczuk, P.; Solla-Gull, J.; Kim, H-S.; Tong, Y.Y.; Montiel, V.; Aldaz, A.; Wieckowski, A. *J. Catalysis*. **2001**, *203*, 1.
- (2) Chen, A.; J, D.; Russa, L.; Miller, B. *Langmuir*. **2004**, *20*, 9695.
- (3) Hamnett, A. in “Interfacial Electrochemistry: Theory, Experiment, and Applications” (A. Wieckowski, Ed.), Dekker, New York., **1999**, p. 843.
- (4) Markovic, N. M.; Gasteiger, H. A.; Ross, Jr., P. N.; Jiang, X.; Villegas, I.; and Weaver, M. J., *Electrochim. Acta*. **1995**, *40*, 91.
- (5) Frelink, T.; Visscher, W.; and van Veen, J. A. R. *Langmuir*. **1996**, *12*, 3702.
- (6) Tian, M.; Wen, J.; MacDonald, D.; Asmussen, R.M.; Chen, A. *Electrochim. Commun.* **2010**, *12*, 527.

- (7) Glavee, G.N.; Klabunde, K. J.; Sorensen, C. M.; Hadjapanayis, G. C. *Langmuir*. **1992**, *8*, 771.
- (8) Park, S-J.; Jung, Y.; Kim, S. *J. Fluorine Chemistry*, **2012**, *144*, 124.
- (9) Chen, S.; Malig, M.; Tian, M.; Chen, A. *J. Phys. Chem. C*. **2012**, *116*, 3298.
- (10) Chrzanowski, W.; Kim, H.; Wieckowski, A. *Catal. Letters*. **1998**, *50*, 69.
- (11) Conway, B. E. *Prog. Surf. Sci.* **1995**, *49*, 331.
- (12) Shi, M.; Zhang, W.; Zhao, D.; Chu, Y.; Ma, C. *Electrochimica Acta*. **2014**, *143*, 222.
- (13) Tremiliosi-Filho, G.; Kim, H.; Chrzanowski, W.; Wieckowski, A.; Grzybowska, B.; Kulesza, P. *J. Electroanal. Chem.* **1999**, *467*, 143.
- (14) Jambunathan, K.; Jayaraman, S.; Hillier, A.C. *Langmuir*. **2004**, *20*, 1856.
- (15) Kim, H.; Tremiliosi-Filho, G.; Haasch, R.; Moraes, I.; Wieckowski, A.; *Surf. Sci. Lett.* **2001**, *474*, L203.
- (16) D. Sebastia, N.; La'zaro, M.J.; Moliner , R.; Suelves, I.; Arico, A.S.; Baglio, V. *Int.J. Hydrogen energy*, **2014**, *39*, 5414.
- (17) J.R.C. Salgado, J.R.C.; Paganin, V.A.; Gonzalez, E.R.; Montemor, M.F.; Tacchini, I.; Anson, A.; Salvador, M.A.; Ferreira, P.; Figueiredo, F.M.L.; Ferreira, M.G.S. *Int.J. Hydrogen energy*, **2013**, *38*, 910.
- (18) Ocampo, A.L.; Jiang, Q-Z.; Ma, Z-F.; Varela, J.R.; Gyves, J.D. *Electrocatalysis*, **2014**, *5*, 387.
- (9) Jiang, Q-Z.; Wu, X.; Shen, M.; Ma, Z-F.; Zhu, X-Y. *Catal. Lett.* **2008**, *124*, 434

- (20) Shen, L.; Jiang, Q-Z.; Gan, T.; Shen, M.; Rodriguez Varela, F.J.; Ocampo, A.L.; Ma, Z-F. *J. New Mater. Electrochem. Syst.* **2008**, *13*, 205.
- (21) Sugimoto, W.; Aoyama, K.; Kawaguchi, T.; Murakami, Y.; Takasu, Y. *J. Electroanalytical Chemistry*. **2005**, *576*, 215.
- (22) Grigorieva, A.V.; Goodilin, E. A.; Derlyukova, L.E.; Anufrieva, T.A.; Tarasov, A.B.; Dobrovolskii, Y.A.; Tretyakov, Y.D. *Applied Catalysis A: General*, **2009**, *362*, 20.
- (23) MacDonald, J.P.; Gualtieri, B.; Runga, N.; Teliz, E.; Zinola, C.F. *Int.J. Hydrogen energy*, **2008**, *33*, 7048.
- (24) Ohanian, M.; Zinola, C.F. *J. Power Sources*, **2007**, *168*, 1:307.

Chapter 5 Modification of TiO₂ Nanotubes with PtRu/Graphene Nanocomposites for Enhanced Oxygen Reduction Reaction

5.1 Introduction

Owing to their environmental compatibility and high efficiency, fuel cells comprise a promising future alternative energy technology to conventional power generating devices.¹⁻³ Within a hydrogen fuel cell, oxygen is reduced at the cathode surface, while hydrogen is oxidized at the anode. The oxygen reduction reaction (ORR) is the key issue and the rate determining step among these two processes, in which oxygen molecules are slow to split and react at the cathode/electrolyte interface (e.g., kinetic sluggishness).⁴⁻⁶ Platinum (Pt) is one of the best ORR catalysts, among other precious metals; however, its activity is still quite low. In addition, Pt dissolves under fuel cell operating conditions,⁷ although Pt catalysts possess some advantages for cathode functionality under very severe conditions, such as low pH, high temperature, oxygen atmosphere, and high humidity, at highly positive potentials, apart from several disadvantages.⁸⁻¹⁰ To further improve their catalytic efficiency and tolerance while decreasing cost, many researchers have tried to develop new techniques for the production of multi-component Pt incorporated catalysts.^{11,12} Catalytic ORR performance has been much improved as a result of the preparation of multi-metallic electrocatalysts with less active precious metals, non-precious catalysts, or enzymatic catalysts, etc.⁵ A further alternative method might be to utilize less expensive noble metals such as ruthenium (Ru) (a stable transition metal), which also possesses appropriate strain and electronic factor effects. Ru has been recognized as an additional electrocatalyst that may be used in ORR.¹³ The interactions between Ru and Pt nanoparticles in the form of an alloy, in conjunction with an underlying substrate, enable the tuning of catalytic ORR properties.¹⁴

To avoid the aggregation, dissolution, and sintering of metal catalysts during ORR, a potential solution might be to anchor/disperse catalysts on specific supports while reducing or even negating the use of capping agents.^{15,16} Graphene comprises a robust two-dimensional (2D) sheet of sp²-hybridized carbon, which has emerged as a most auspicious substrate.¹⁷ It comprises an ideal platform for the growth or anchoring of functional nanomaterials, such as metallic and semiconducting nanoparticles, by providing a blend of its high surface area, enhanced mobility of charge carriers, and good stability.¹⁸ Moreover, graphene creates exceptional catalytic activity through increased charge transfer from resident metallic nanoparticles to the substrate.¹⁹ The synthesis of nanostructured metallic particles on stable and inexpensive substrates has attracted much attention in recent research studies.²⁰ For example, TiO₂ substrates provide several advantages due to their low cost, easy fabrication and high stability.²¹ In particular, TiO₂ nanotubes have become of primary interest due to their relevant photocatalytic and electrocatalytic applications as an excellent substrate.²²⁻²⁴ The control of the composition and morphology of nanostructured metallic particles on supported conductive substrates through electrochemical deposition has garnered much interest for the fabrication of basic nanostructures to practical devices, as it has been found to constitute a simple, low-cost, and time-saving process.²⁵⁻²⁷

Herein, we have demonstrated a single-step electrochemical synthesis of rGO-PtRu nanocomposites on a TiO₂NT substrate, where the composition and structure of the Pt and Ru nanoparticles within the rGO nanocomposites were organized by controlling the concentrations of the precursors and the duration of the applied potential. The developed electrochemical synthesis of rGO-PtRu nanocomposites on TiO₂NT has intrinsic advantages. Our electrochemical

studies have shown that the fabricated TiO₂NT/rGO-PtRu (64:36) nanocomposite electrode exhibited an excellent electrocatalytic activity for ORR.

5.2 Experimental and Methods

Ti (99.2%) plates (1.25 cm × 0.80 cm × 0.5 mm) were cleaned via sonication in acetone, followed by pure water (18.2 MΩ cm), and then etched in an 18% HCl solution at 85°C for 15 min, and finally rinsed with pure water. The TiO₂NTs were prepared in a dual-electrode electrochemical cell, where an etched Ti plate was used as the working electrode and a Pt plate was used as the counter electrode. The Pt plate was cleaned prior to each experiment by flame-annealing. The anodization took place in a solution that consisted of dimethyl sulfoxide (DMSO) with 2% (wt) HF at 40 V for 8 h. The sample was annealed at 450 °C for 3 h to form an anatase structured TiO₂NT followed by UV pretreatment using a quartz tube, within which was placed a TiO₂ sample with 5 mL of 50% methanol-H₂O (v/v). Ar was purged for 5 min and irradiated under UV light for 60 min.²⁸ A series of PtRu nanoparticles with various compositions were electrochemically prepared with GO onto TiO₂NT substrates. Four different compositions of rGO-PtRu nanocomposites were synthesized from H₂PtCl₆ and RuCl₃ with encompassing the Pt:Ru ratio of 84:16, 69:31, 64:36, and 42:58 based on the EDX analysis, respectively. Each composition was combined with 0.05 mg/mL of GO in the precursor solutions and reserved as constants for the preparation of the nanocomposites. The electrochemical deposition was carried out at an applied potential of -1.0V (vs Ag/AgCl) for 1000 s in 0.5 M H₂SO₄. The electrode was subsequently removed from the solution, rinsed with ultrapure water, and dried in an oven at 40 °C.

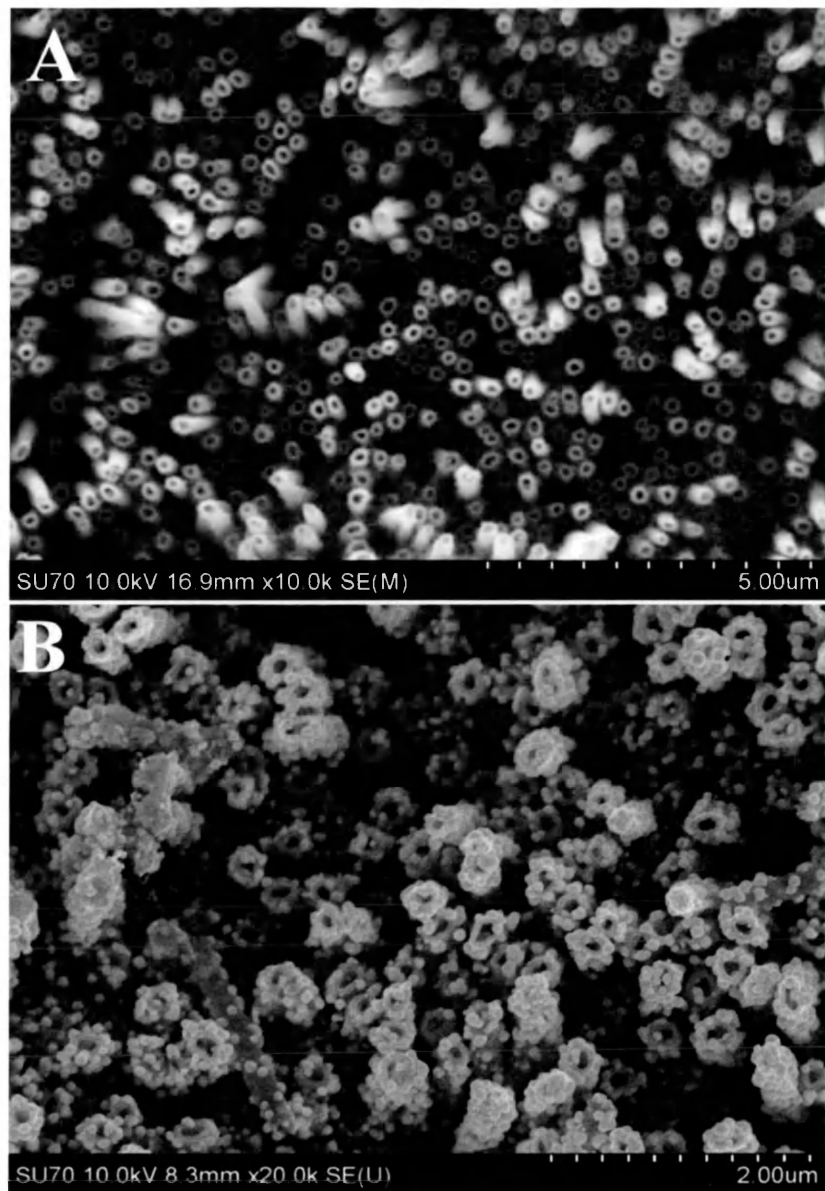


Figure 5.1. SEM images of the TiO₂NTs (A) and TiO₂NT/rGO-PtRu (64:36) electrode (B).

5.3 Surface morphology and compositions of Pt-Ru catalysts

The surface morphology and composition of the TiO₂NT/rGO-PtRu nanocomposite electrodes were examined using SEM and EDS techniques. Figure 5.1 A and B depict the SEM images of the TiO₂NTs and the TiO₂NT/ rGO-Pt:Ru(64:36) nanocomposite, respectively. Uniform TiO₂NTs were grown onto the Ti substrate employing the electrochemical anodic oxidation. The median dimension of the PtRu nanoparticles was estimated to be ~40 nm in diameter, which were well dispersed on the as-prepared TiO₂NTs. The diameter of these nanotubes was estimated to be ~145 nm with wall thicknesses of ~20 nm. The EDS spectra are displayed in Figure 5.2A, where the atomic ratios of Pt to Ru, calculated from the EDS measurements, were, 84:16 (curve a), 69:31 (curve b), 64:36 (curve c) and 42:58 (curve d), respectively, for the four TiO₂NT/rGO-PtRu electrodes. Figure 2B - D depict the elemental mapping of Pt, Ru, and C on the TiO₂NT substrate, respectively, revealing that the PtRu nanoparticles were homogeneously dispersed and that the composition of the rGO-PtRu nanocomposite formed on the TiO₂NTs was successfully controlled by the facile electrochemical deposition method employed in the present study.

The crystalline nature of the TiO₂NT/rGO-PtRu nanocomposites was characterized by the XRD technique. Figure 5.3 shows the XRD patterns of the rGO-PtRu nanocomposite with different ratios of Pt:Ru (84:16, curve a; 69:31, curve b; 64:36, curve c; and 42:58, curve d) deposited on the TiO₂NTs, where the peaks marked with asterisks were derived from the Ti of the anatase TiO₂NTs. The PtRu nanoparticles exhibited diffraction peaks at 46.6, 67.7, and 82.6°, corresponding to the characteristic (200), (220), and (311) plane reflections of a Pt face-centered cubic (fcc) structure (JCPDS file no. 4-0802).²³ The XRD patterns of the nanocomposites

displayed in Figure 5.3 show that no distinct Pt and Ru peaks were obtained, indicating the formation of PtRu alloys without crystalline Pt and Ru metal phase separation.

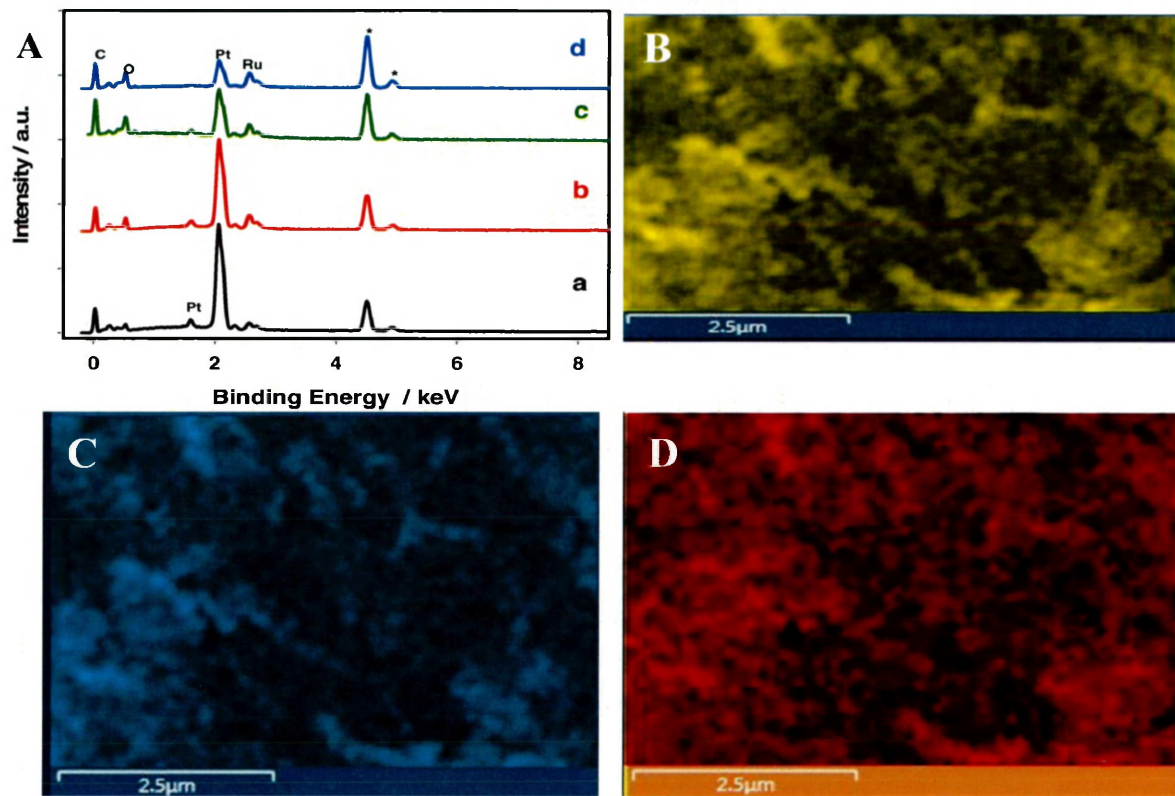


Figure 5.2. (A) EDS of the $\text{TiO}_2\text{NT}/\text{rGO-PtRu}$ electrodes with their composition of Pt:Ru 84:16 (a), 69:31 (b), 64:36 (c) and 42:58 (d) in the nanocomposites on the TiO_2NT (Peaks marked with asterisks are derived from Ti). Elemental mapping of the Pt (B), Ru (C) and C (D) obtained at the $\text{TiO}_2\text{NT}/\text{rGO-PtRu}$ (64:36) electrode.

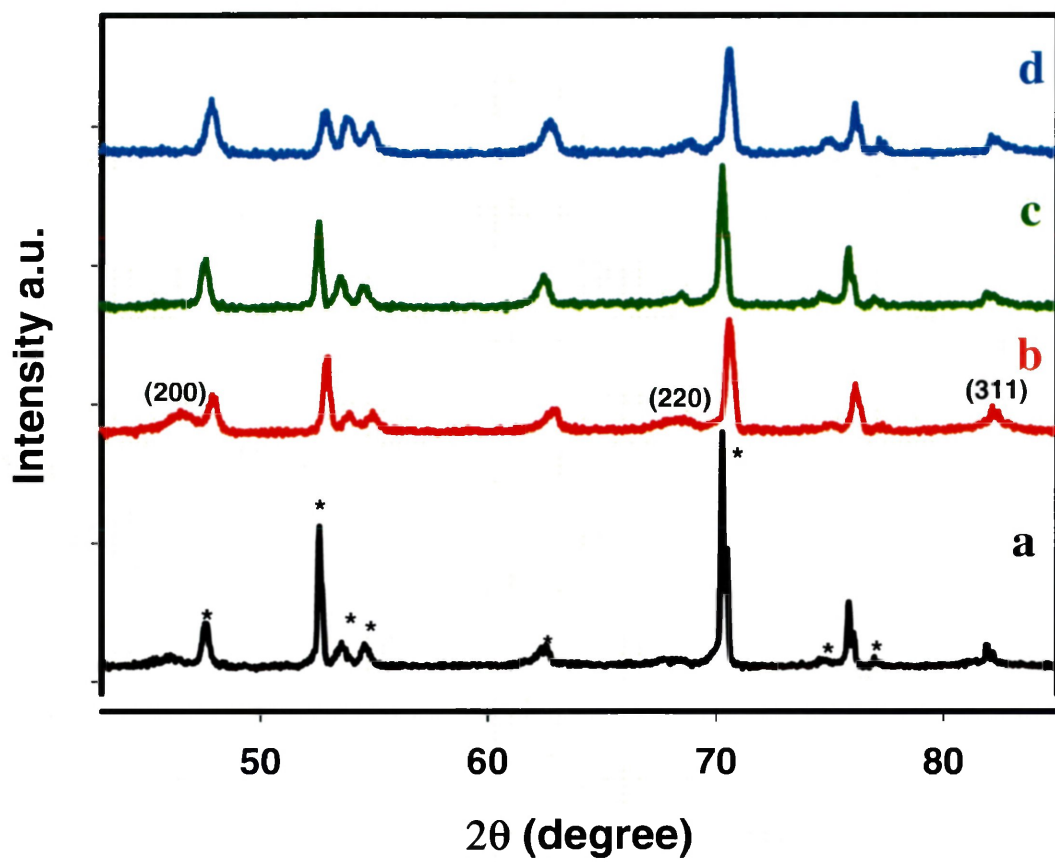


Figure 5.3. XRD of the $\text{TiO}_2\text{NT}/\text{rGO-PtRu}$ electrodes with their composition of Pt:Ru 84:16 (a), 69:31 (b), 64:36 (c) and 42:58 (d) in the nanocomposites on the TiO_2NT (Peaks marked with asterisks are derived from the anatase phase of TiO_2).

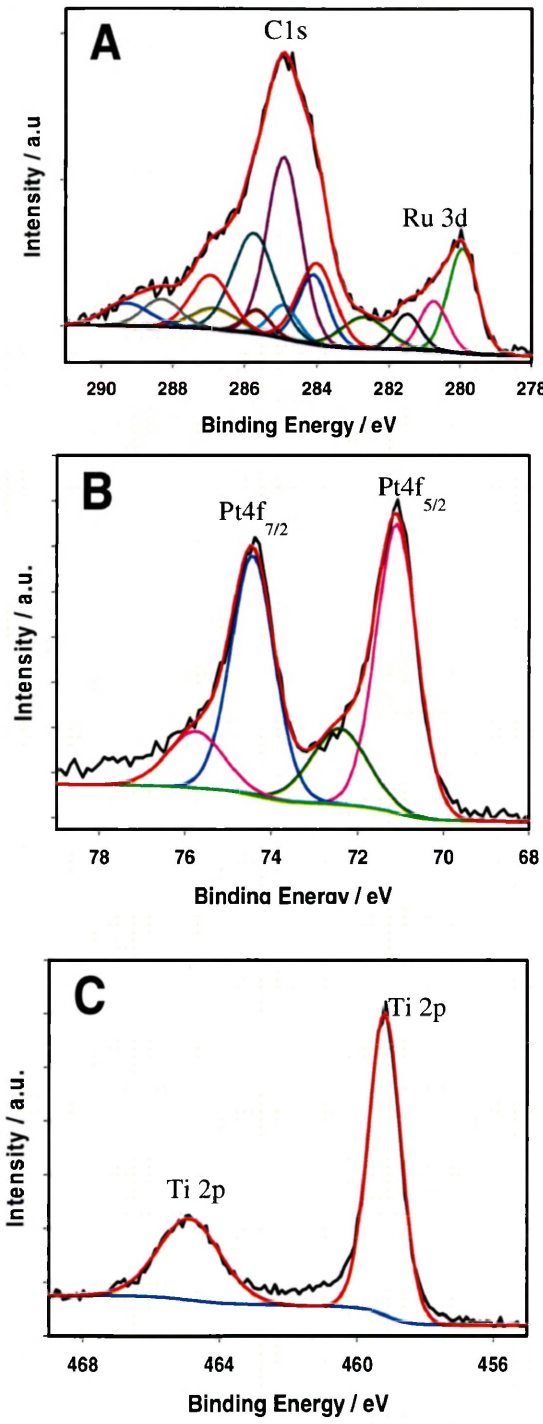


Figure 5.4. XPS spectra of the C 1s and Ru 3d regions (A), Pt 4f region (B) and Ti 2p region (C) for the TiO₂NT/rGO-PtRu nanocomposite.

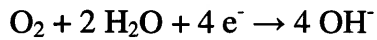
XPS was employed to further characterize the chemical states of the elements in the TiO₂NT/rGO-PtRu nanocomposites. Figure 5.4 shows the curve fitting and deconvolution of Ru3d, C1s, Pt4f, and Ti2p peaks of the XPS spectra of the as-prepared TiO₂NT/rGO-PtRu (64:36) nanocomposite electrode. It is known that Ru 3d peaks overlap with the C 1s peaks. As shown in Figure 5.4A, the C1s-Ru3d core level spectrum exhibits several peaks that are centered at binding energies of 284.90 and 280.00 eV. The binding energies of the C 1s core level are highly dependent on the position of the related atoms within the chemical structure. The C1s peaks at 284.90, 285.74, 286.94, 288.31 and 289.29 eV were obtained for sp² C, C-OH, C-O, C=O and HO-C=O, respectively. As shown in Figure 4A, the decrease of the oxygen containing functional groups of the C-O, C=O and HO-C=O peaks at 286.94, 288.31 and 289.29 eV in comparison with GO indicated the effective electrochemical deposition of graphene on the TiO₂NT surface. The slight shift of C 1s peaks to the higher binding energy, in contrast to previous reports, indicated that the metals were dispersed on the rGO surface^{29,30} GO. The Ru 3d peaks at 279.93, 280.73, 281.48, and 282.68 eV were observed for the binding energy that was associated with Ru 3d_{5/2} electrons, whereas the other peaks, at 284.10, 284.90, 285.65, and 286.85 eV, corresponded to the binding energy associated with Ru 3d_{3/2} electrons. The Ru 3d peaks at 279.93 and 280.73 eV for Ru 3d_{5/2} and at 284.10 and 284.90 eV for Ru3d_{3/2} respectively, were associated with metallic Ru. The other peaks at 281.48 and 282.68 eV for Ru 3d_{5/2}, and 285.65 and 286.85 eV for Ru 3d_{3/2}, respectively, corresponded to the Ru oxide.³¹ The percentages of the metallic and oxide states of Ru were estimated on the basis of the integration of their individual metallic/oxide components, as well as the total components. It was estimated to be 65.35% and 34.65% of metallic Ru and Ru oxide, respectively, indicating that Ru was partially within the localized TiO₂ and graphene environments. As displayed in Figure 5.4B, Pt 4f signal contained intense doublet peaks, at 71.09 and 74.42 eV, for 4f_{5/2} and 4f_{7/2} electrons, respectively,

with an asymmetric nature, corresponding to metallic Pt. In addition, less intense peaks, at 72.43 and 75.75 eV for $4f_{5/2}$ and $4f_{7/2}$ electrons, respectively, were observed with a doublet peak energy separation of about 3.32 eV, suggesting the presence of a small Pt(II) fraction. The Pt peaks of the TiO₂NT/rGO-PtRu nanocomposite electrode displayed a shift of Pt 4f binding energy to the high energy direction by 0.9 eV, in comparison to previous reports.³² The shift in these peaks indicated a strong metal-support interaction between the Pt and TiO₂NTs/rGO.³³ The percentages of the metallic Pt and Pt oxides were calculated via the integration of their individual metallic components and total components. It was found that there were 75.07% of metallic Pt and 24.93% of Pt oxide, suggesting that Pt was also partially oxidized. The actual atomic composition of Pt and Ru was calculated based on the integrated area under the peaks, to be 61:39% Pt:Ru, which is close to the ratio estimated from the EDS analysis. Figure 5.4C presents the XPS fitting curve for the Ti 2p peak, showing two Gaussians, centered at 459.19 and 464.87 eV, which were associated with pure anatase TiO₂. A high binding energy shift of about 1.6 eV was observed for Ti 2p, which indicated the interaction of PtRu nanoparticles with anatase TiO₂.³³

5.4. Electrochemistry behaviour of the TiO₂NT/rGO-PtRu nanostructures

The electrocatalytic activity of the TiO₂NT/rGO-PtRu (64:36) nanocomposite was investigated via the electrocatalytic reduction of oxygen in an alkaline media at room temperature. Figure 5.5 shows the cyclic voltammograms (CVs) of the TiO₂NTs (magenta line), TiO₂NT/rGO (blue line), TiO₂NT/rGO-Ru (red line), TiO₂NT/rGO-Pt (black line), TiO₂NT/PtRu (cyan line), and TiO₂NT/rGO-PtRu (64:36) modified electrodes recorded in the range between 0.2 V and -0.4V in O₂-saturated 0.1 M KOH at a scan rate of 20 mVs⁻¹. There was almost no response observed at the TiO₂NT (magenta) and TiO₂NT/rGO (blue) electrodes. The small reduction waves with onset potentials of -0.17V and -0.15V and the current densities of 0.4

mA cm^{-2} and 0.8mA cm^{-2} , at the reduction potential of -0.4V, were obtained for the $\text{TiO}_2\text{NT/rGO-Pt}$ and $\text{TiO}_2\text{NT/rGO-Ru}$ electrodes, respectively, toward ORR in 0.1 M KOH. The well-defined cathodic reduction waves observed for the $\text{TiO}_2\text{NTs/PtRu}$ nanoparticles (cyan) and for the $\text{TiO}_2\text{NT/rGO-PtRu}$ nanocomposite (green), respectively, with an onset potential of -0.02V for both electrodes. Current densities of 0.8 mA cm^{-2} and 1.6 mA cm^{-2} were attained at the $\text{TiO}_2\text{NT/PtRu}$ nanoparticle electrode (cyan), and the $\text{TiO}_2\text{NT/rGO-PtRu}$ nanocomposite electrode (dark green), respectively, as seen in Figure 5. It was clear that the ORR activity observed for the $\text{TiO}_2\text{NT/rGO-PtRu}$ (64:36) nanocomposite electrode was approximately double that of the $\text{TiO}_2\text{NT/PtRu}$ (64:36) electrode, as displayed in Figure 5.5. It is interesting to understand the reaction mechanism of the ORR process at the electrocatalyst and the resulting effects for use in fuel cell systems. The ORR in the alkaline medium primarily favored the four-electron pathway at the PtRu electrocatalyst, and the possible reaction pathways have been previously reported.³⁴ The initial rate determining step involved the $2e^-$ reduction of O_2 and the consumption of H_2O to form the intermediate reaction products, HO_2^- and OH^- . In the second step, the peroxide radical (HO_2^-) could be further reduced, via an additional $2e^-$, to form OH^- , with the overall reaction:



The optimization of the $\text{TiO}_2\text{NT/rGO-PtRu}$ nanocomposite was carried out by monitoring the ORR activity in 0.1 M KOH, shown in Figure 5.6. The CVs were recorded for the different Pt:Ru compositions (84:16, 69:31, 64:36, 42:58), respectively, on the $\text{TiO}_2\text{NT/rGO}$ electrodes in O_2 -saturated 0.1 M KOH at a scan rate of 20 mV/s. The ORR activity depended on the composition of the PtRu nanoparticles. The highest cathodic current density was attained at approximately -1.7 mA cm^{-2} at -0.4V for the $\text{TiO}_2\text{NT/rGO-PtRu}$ (64:36) nanocomposite.

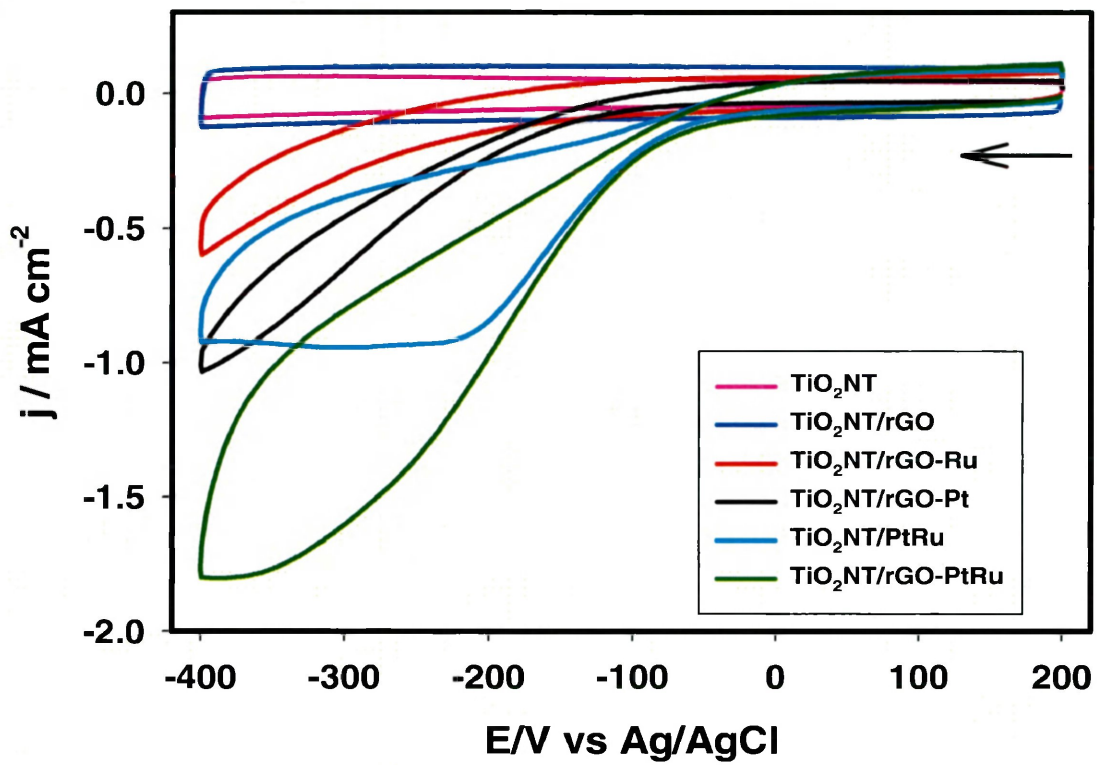


Figure 5.5. CVs of the TiO_2NT (magenta), $\text{TiO}_2\text{NT/rGO}$ (blue), $\text{TiO}_2\text{NT/rGO-Pt}$ (red), $\text{TiO}_2\text{NT/rGO-Ru}$ (black), $\text{TiO}_2\text{NT/PtRu}$ (cyan) and $\text{TiO}_2\text{NT/rGO-PtRu}$ (60:40) (green) electrodes recorded in O_2 -saturated 0.1 M KOH, scan rate of 20 mV/s.

On a further increase in the amount of Ru in the PtRu (42:58) composition, the ORR activity was slightly decreased when compared to other composite electrodes in the present investigation, as shown in Figure 6. Table 1 presents the ORR catalytic activity of the prepared TiO₂NT/rGO-PtRu electrodes, indicating that TiO₂NT/rGO-PtRu (64:36) electrode exhibited the highest catalytic activity toward ORR in alkaline medium when compared to the other electrodes that were prepared in this study. The high-performance catalytic ORR activity of the TiO₂NT/rGO-PtRu (64:36) electrode was obtained by modifying the electronic properties of Pt through the Pt-Ru orbital overlap within the graphene composite. The TiO₂NT/rGO-PtRu (64:36) electrode demonstrated an enhanced ORR electrocatalytic activity in decreasing the overpotential and augmenting the current density compared to other electrodes, as displayed in Table 5.1. These electrocatalytic results indicated that the present TiO₂NT/rGO-PtRu (64:36) electrode exhibited superior ORR activity in terms of decreasing overpotential over the electrocatalysts reported in the literature, including Pt/C, demonstrating that the electrocatalytic activity for ORR in 0.1M KOH was associated with a more positive ORR onset, as shown in Table 5.2.^{18,35-43} The excellent ORR catalytic activity of the TiO₂NT/rGO-PtRu (64:36) electrode that was attained in the present study might be associated to the uniformly dispersed PtRu nanoparticles on the surface of the TiO₂NT, as well as the combination of the graphene sheets, providing a synergistic coupling effect toward outstanding ORR activity.

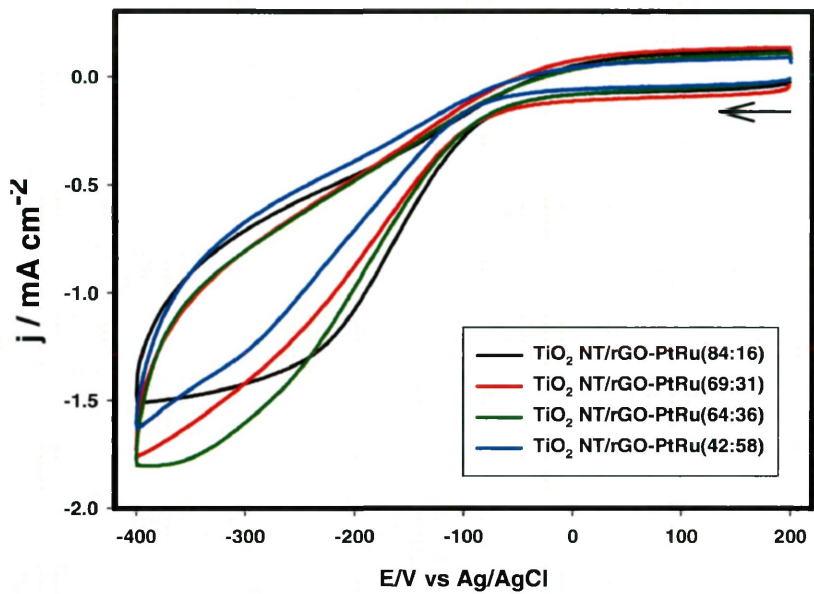


Figure 5.6. CVs of the $\text{TiO}_2\text{NT}/\text{rGO-PtRu}$ electrodes with their composition of Pt:Ru (84:16, black), (69:31, red), (64:36, green) and (42:58, blue) in the nanocomposites on the TiO_2NT electrodes recorded in O_2 -saturated 0.1 M KOH, scan rate of 20 mV/s.

Table 5.1. List of the ORR activities of the fabricated $\text{TiO}_2\text{NT}/\text{rGO-PtRu}$ electrodes.

Electrodes	Onset Potential/V (Ag/AgCl)	Reduction Potential/V (Ag/AgCl)	Current Density/ mA cm^{-2} (@-0.32V)
$\text{TiO}_2\text{NT}/\text{rGO-PtRu}(84:16)$	-0.039	-0.254	-1.386
$\text{TiO}_2\text{NT}/\text{rGO-PtRu}(69:31)$	-0.002	-0.325	-1.436
$\text{TiO}_2\text{NT}/\text{rGO-PtRu}(64:36)$	0.007	-0.334	-1.617
$\text{TiO}_2\text{NT}/\text{rGO-PtRu}(42:58)$	-0.058	-0.293	-1.280

Table 5.2. Comparison of the onset potential values of different ORR catalysts.

Electrocatalysts	ORR Onset Potential/V (vs Ag/AgCl)	Electrolyte	References
MnFe ₂ O ₄	-0.18	0.1 M KOH	35
Pt/C	-0.13	0.1 M KOH	36
HU-Graphene	-0.14	0.1M KOH	37
BCN graphene	-0.13	0.1M KOH	38
Ag/MWCNT	-0.16	0.1M KOH	39
Au/SnO ₂	-0.16	0.02M NaOH	40
N-Graphene	-0.13	0.1M KOH	41
AgNps	-0.17	0.1M NaClO ₄	42
Ni ₃ C	-0.30	0.1M H ₂ SO ₄	43
Au/rGO	-0.03	0.1M KOH	18
TiO₂NT/rGO-PtRu(64:36)	0.01	0.1M KOH	Present Work

To further investigate the activity of the TiO₂NT/rGO-PtRu electrodes with different Pt:Ru compositions in the nanocomposites, electrochemical impedance spectroscopy (EIS) was used for ORR in 0.1 M KOH. Figure 5.7 displays the EIS of the TiO₂NT/rGO-PtRu electrodes with the composition of Pt:Ru 84:16 (curve a), 69:31 (curve b), 64:36 (curve c), and 42:58 (curve d) in the nanocomposites, which was recorded for ORR in 0.1 M KOH at the applied potential of -0.25V. These impedance results were fitted as solid lines with an equivalent electric circuit. The equivalent electric circuit that was used to fit with the experimental data is shown in the inset of Figure 5.7. R_s denotes solution resistance, R_p represents the parallel combination of the charge-transfer resistance, and CPE characterizes the constant ORR phase element. The CPE is defined by CPE-T and CPE-P, and the CPE is considered to be a capacitor (C_{dl}) if CPE-P is equal to 1. Table 5.3 depicts the values of all the parameters of R_s, R_p, CPE-T, CPE-P and their associated percentage errors determined by the fitting of the experimental EIS data. All of the associated errors listed in Table 5.3 are within 5%, suggesting that the electric equivalent circuit used (shown in Figure 5.7) may effectively fit the experimental data. The CPE-P values for the nanocomposite electrodes was ~ 0.9, indicating that the CPE-T values obtained in this study are close to C_{dl}, as can be seen in Table 5.3. The R_s values for all of the nanocomposite electrodes were in the range of 7.5 to 8.9 Ω, and the R_p values were varied with different electrode compositions. The R_p values were decreased from 627.2 Ω to 208.8 Ω by increasing the amount of Ru in the PtRu nanoparticles from 16% to 36%; However, the R_p value was increased to about 220.9 Ω at the TiO₂NT/rGO-PtRu (42:58) electrode. The CPE-T values were 3.4, 3.9, 4.2 and 3.2 mF cm⁻² for the rGO-PtRu (84:16), rGO-PtRu (69:31), rGO-PtRu (64:36) and rGO-PtRu (42:58) compositions on the TiO₂NT electrodes. The TiO₂NT/rGO-PtRu (64:36) electrode exhibited the smallest R_p value and the largest CPE-T value among all the fabricated nanocomposites in the

present study, as shown in Table 5.3, which are consistent with the results observed in Figure 5.5 and Figure 5.6.

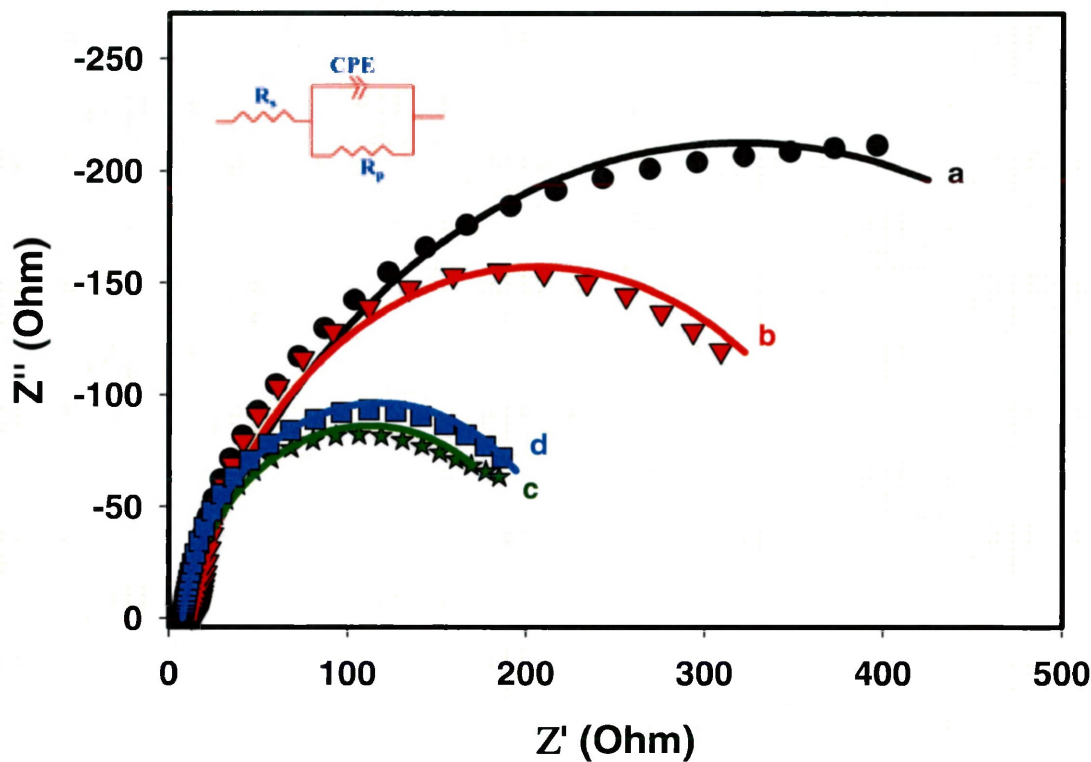


Figure 5.7. Nyquist plots of the $\text{TiO}_2\text{NT}/\text{rGO-PtRu}$ electrodes with their composition of Pt:Ru 84:16 (a), 69:31 (b), 64:36 (c) and 42:58 (d) in the nanocomposites on the TiO_2NT electrodes recorded in O_2 -saturated 0.1 M KOH. The amplitude of modulation potential was 5 mV. The frequency was altered, from 100 kHz to 40 mHz with the applied potential of -0.25V. Inset: The corresponding equivalent electric circuit.

Table 5.3. EIS data of the TiO₂NT/rGO-PtRu electrodes with different compositions of Pt:Ru obtained from the Nyquist plots of Figure 5.4.

Electrodes	Rs ($\Omega \text{ cm}^2$)		R_p ($\Omega \text{ cm}^2$)		CPE-T (mF.cm^{-2})		CPE-P	
	Value	Error (%)	Value	Error (%)	Value	Error (%)	Value	Error (%)
TiO ₂ NT/rGO-PtRu(84:16)	7.5	1.9	627.2	4.6	3.4	3.5	0.8	1.6
TiO ₂ NT/rGO-PtRu(69:31)	8.9	0.9	384.9	2.6	3.9	2.3	0.9	1.0
TiO ₂ NT/rGO-PtRu(64:36)	8.1	0.5	208.8	1.1	4.2	1.3	0.9	0.5
TiO ₂ NT/rGO-PtRu(42:58)	7.6	1.2	220.9	2.1	3.2	2.0	0.9	1.1

The durability of the TiO₂NT/rGO-PtRu (64:36) nanocomposite electrode was further tested for ORR in alkaline media. The amperometric i-t curve was recorded to monitor the stability of the present composite electrode by applying -0.35 V in O₂-saturated 0.1 M KOH for 50,000 s, which is displayed in Figure 5.8 as the relative current density in the percentage scale. It is interesting to note that the current density at the TiO₂NT/rGO-PtRu (64:36) electrode revealed a slow decay during the ORR. Subsequent to the testing of the nanocomposite electrode over 50,000 s, a loss in the cathodic current density of ~ 9% occurred, as shown in Figure 8, showing that the TiO₂NT/rGO-PtRu (64:36) nanocomposite electrode possessed high stability as a novel ORR electrocatalyst.

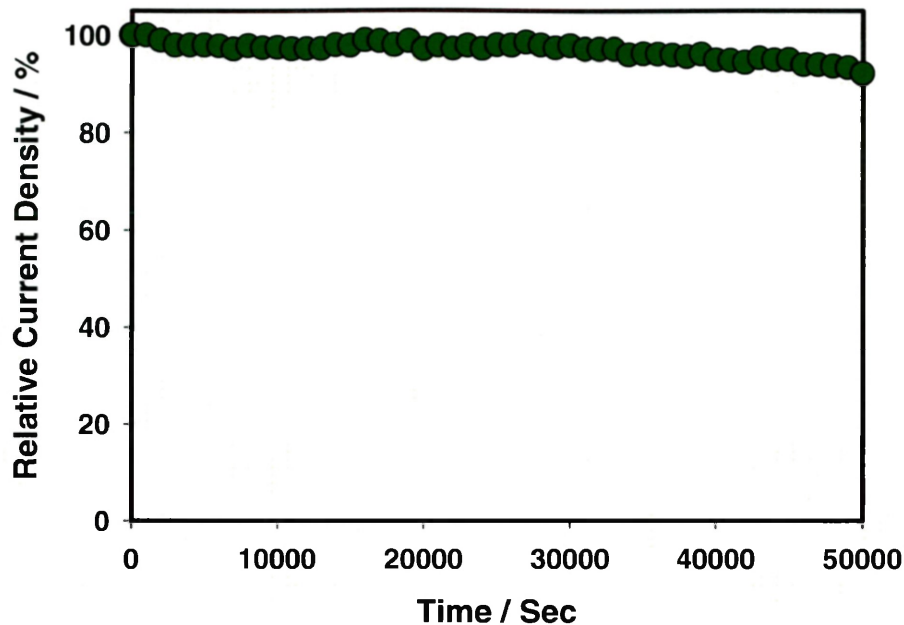


Figure 5.8. Amperometric i-t response obtained for ORR at the TiO₂NT/rGO-PtRu electrode with E_{app} of -0.35V in O₂-saturated 0.1M KOH.

5.5. Conclusions

In conclusion, we have successfully fabricated novel TiO₂NT/rGO-PtRu nanocomposites through a single-step electrochemical deposition method. The prepared TiO₂NT/rGO-PtRu (64:36) nanocomposite electrode exhibited a high ORR activity in 0.1 M KOH solution. The superior electrocatalytic performance of the TiO₂NT/rGO-PtRu (64:36) nanocomposite electrode was primarily attributed to the intrinsic catalytic activity of the PtRu nanoparticles, with potent rGO and TiO₂NT interactions via improved charge transport through the rGO sheets, thus leading to a high ORR performance. The TiO₂NT/rGO-PtRu (64:36) electrocatalyst developed in the present study also possessed long-term durability. Moreover, the facile approach reported here may serve as a forerunner for the design of variety of advanced hybrid TiO₂NT/graphene-metal nanoparticle catalysts, which may enable a broad range of environmental and energy applications.

References

- (1) Aravind, S. S.; Ramaprabhu, S. *ACS Catal.* **2012**, *4*, 3805.
- (2) Wang, S.; Zhang, L.; Xia, Z.; Roy, A.; Chang, D. W.; Baek J-B.; Dai, L. *Angew. Chem. Int. Ed.* **2012**, *51*, 4209.
- (3) Kim, S. S.; Kim, Y. R.; Chung, T. D.; Sohn, B. H. *Adv. Funct. Mater.* **2014**, *24*, 2764.
- (4) Lee, Y. J.; Hsieh, Y. C.; Tsai, H. C.; Lu, I. T.; Wu, Y. H.; Yu, T.; Lee, J. F.; Merinov, B.; Goddard, W.; Wu, P. W. *Science* **2014**, *150*, 636.
- (5) Guo, S.; Zhang, S.; Su, D.; Sun, S. *J. Am. Chem. Soc.* **2013**, *135*, 13879.
- (6) Wang, X.; Wang, .; Wang, D.; Dou, S.; Ma, Z.; Wu, J.; Tao, L.; Shen, A.; Ouyang, C.; Liu, Q.; Wang, S. *Chem. Commun.* **2014**, *50*, 4839.
- (7) Chen, H. S.; Liang, Y. T.; Chen, T. Y.; Tseng, Y. C.; Liu, C. W.; Chung, S. R.; Hsieh, C. T.; Lee, C. E.; Wang, K. W. *Chem. Commun.* **2014**, *50*, 11165.
- (8) Holt-Hindle, P.; Yi, Q.; Wu, G.; Koczkur, K.; Chen, A. *J. Electrochem. Soc.* **2008**, *155*, K5-K9.
- (9) Alia, S. M.; Pylypenko, S.; Neyerlin, K. C.; Cullen, D. A.; Kocha, S. S.; Pivovar, B. S. *ACS Catal.* **2014**, *4*, 2680.
- (10) Arroyo-Ramírez, L.; Rodríguez, D.; Otaño, W.; Cabrera, C. *ACS Catal.* **2012**, *4*, 2018-2024.
- (11) Yang, J.; Yang, J.; Ying, J. Y. *ACS Nano* **2012**, *6*, 9373.
- (12) Liu, C. W.; Chen, H. S.; Lai, C. M.; Lin, J. N.; Tsai, L. D.; Wang, K. W. *ACS Appl. Mater. Interfaces* **2014**, *6*, 1589.
- (13) Yang, L.; Vukmirovic, M. B.; Su, D.; Sasaki, K.; Herron, J. A.; Mavrikakis, M.; Liao, S.; Adzic, R. R. *J. Phys. Chem. C* **2013**, *117*, 1748.
- (14) Zhang, J.; Vukmirovic, M. B.; Xu, Y.; Mavrikakis, M.; Adzic, R. R. *Angew. Chem. Int. Ed.* **2005**, *44*, 2132.

- (15) Wang, Y. J.; Wilkinson, D. P.; Zhang, J. *Chem. Rev.* **2011**, *111*, 7625.
- (16) Yin, H.; Tang, H.; Wang, D.; Gao, Y.; Tang, Z. *ACS Nano* **2012**, *6*, 8288.
- (17) Geim, A. K.; Novoselov, K. S. *Nat. Mater.* **2007**, *6*, 183.
- (18) Govindhan, M.; Chen, A. *J. Power Sources* **2015**, *274*, 928.
- (19) Kamat, P. V. *J. Phys. Chem. Lett.* **2010**, *1*, 520.
- (20) Ji, X.; Lee, K. T.; Holden, R.; Zhang, L.; Zhang, J. J.; Botton, G. A.; Couillard, M.; Nazar, L. F. *Nat. Chem.* **2010**, *2*, 286.
- (21) Wu, G.; Nishikawa, T.; Ohtani, B.; Chen, A. *Chem. Mater.* **2007**, *19*, 4530.
- (22) Chen, S.; Malig, M.; Tian, M.; Chen, A. *J. Phys. Chem. C* **2012**, *116*, 3298.
- (23) Chang, X.; Thind, S. S.; Chen, A. *ACS Catal.* **2014**, *4*, 2616.
- (24) Tian, M.; Wu, G.; Chen, A. *ACS Catal.* **2012**, *2*, 425.
- (25) Chen, A.; Holt-Hindle, P. *Chem. Rev.* **2010**, *110*, 3767.
- (26) Chen, A.; Chatterjee, S. *Chem. Soc. Rev.* **2013**, *42*, 5425.
- (27) Adhikari, B.; Govindhan, M.; Chen, A. *Electrochimica Acta* **2014** *In Press*.
- (28) Tian, M.; Thind, S. S.; Chen, S.; Matyasovszky, N.; Chen, A. *Nanotechnology* **2012**, *23*, 475.
- (29) Wagner, C. D.; Riggs, W. M.; Davis, L. E.; Moulder, J. F.; Muilenberg, G. E. *Handbook of X-ray Photoelectron Spectroscopy*, Perkin-Elmer Corporation, **1979**.
- (30) Dillon, E. P.; Crouse, C. A.; Barron, A. R. *ACS Nano* **2008**, *2*, 156.
- (31) Paoli, E. A.; Masini, F.; Frydendal, R.; Deiana, D.; Schlaup, C.; Malizia, M.; Hansen, T. W.; Horch, S.; Stephens, I. E. L.; Chorkendorff, I. *Chem. Sci.* **2015**, *6*, 190.
- (32) Xia, B. Y.; Wang, J. N.; Teng, S. J.; Wang, X. X. *Chem.-Eur. J.* **2010**, *16*, 8268.
- (33) Xia, B. Y.; Wang, B.; Wu, H. B.; Liu, Z.; Wang, X.; Lou, X. W. *J. Mater. Chem.* **2012**, *22*, 16499.

- (34) Olson, T. S.; Pylypenko, S.; Atanassov, P.; Asazawa, K.; Yamada, K.; Tanaka, H. *J. Phys. Chem. C* **2010**, *114*, 5049.
- (35) Zhu, H.; Zhang, S.; Huang, Y.-X.; Wu, L.; Sun, S. *Nano Lett.* **2013**, *13*, 2947.
- (36) Lv, J.-J.; Feng, J. X.; Li, S. S.; Wang, Y. Y.; Wang, A. J.; Zhang, Q. L.; Chen, J. R.; Feng, J. *J. Electrochimica Acta* **2014**, *133*, 407.
- (37) Wang, L.; Ambrosi, A.; Pumera, M. *Angew. Chem. Int. Ed.* **2013**, *52*, 13818.
- (38) Wang, S.; Zhang, L.; Xia, Z.; Roy, A.; Chang, D. W.; Baek, J. B.; Da, L. *Angew. Chem. Int. Ed.* **2012**, *51*, 4209.
- (39) Cheng, Y.; Li, W.; Fan, X.; Liu, J.; Xu, W.; Yan, C. *Electrochim. Acta* **2013**, *111*, 635.
- (40) Chen, W.; Ny, D.; Chen, S. *J. Power Sources* **2010**, *195*, 412.
- (41) Vikkisk, M.; Kruusenberg, I.; Joost, U.; Shulga, E.; Kink, I.; Tammeveski, K. *Appl. Catal. B: Environ.* **2014**, *147*, 369.
- (42) Neumann, C. C. M.; Laborda, E.; Tschulik, K.; Ward, K. R.; Compton, R. G. *Nano Res.* **2013**, *6*, 511.
- (43) Su, Y.; Zhu, Y.; Yang, X.; Shen, J.; Lu, J.; Zhang, X.; Chen, J.; Li, C. *Ind. Eng. Chem. Res.* **2013**, *52*, 6076.

Chapter 6 Summary and future work

The unique catalytic activity of PtIr and PtRu nanoparticles investigated in this thesis are considered to be the most effective catalysts for enhancement of fuel cells. Essentially, Pt-, Ir-, and Ru based nanomaterials have the potential for being used to develop more efficient catalysts in DMFCs. There are two different methods employed in the synthesis of the PtIr and PtRu nanomaterials in this work: (1) chemical reduction, and (2) electrochemical deposition/reduction. All synthesized nanomaterials were characterized using surface analysis techniques and electrochemical methods.

6.1 PtIr nanoparticles deposited on TiO₂NTs for DMFC

DMFCs represent a potential alternative to conventional energy generating devices. Methanol as a fuel source for DMFCs has several advantages over other fuels, such as high availability, high energy conversion efficiency, and high energy density. Moreover, DMFCs themselves allow for easier distribution in comparison to other energy generating devices.

Pt is commonly used as an electrocatalyst in DMFCs; however, there are limitations, as it is very expensive and readily poisoned by partial oxidation products (i.e., CO) in the methanol oxidation reaction. Thus, there is interest in doping Pt with other metals to reduce costs and CO poisoning. In Chapter 3, the synthesis of PtIr nanoparticles on TiO₂NT was achieved using the chemical reduction technique. SEM results indicated that the chemical reduction method, which used a sodium borohydride as the reduction agent at room temperature, effectively controlled the distribution of PtIr nanoparticles. PtIr nanoparticles were uniformly distributed with a small particle sizes of ~10 to 18 nm. Moreover, EDX results confirmed the Pt and Ir composition. The electrochemical results presented in Chapter 3 demonstrated that increasing the relative

composition of Ir in the PtIr mixture increased oxidation peaks. The 60:40 composition of PtIr showed the highest methanol oxidation activity.

6.2 PtRu nanoparticles deposited on TiO₂NTs for DMFC

In Chapter 4, a series of PtRu nanoparticles with different compositions were synthesized and successfully deposited onto TiO₂NT substrates via the chemical reduction method. TiO₂ nanotubes were easily synthesized using the electrochemical anodic oxidation method. The formed TiO₂NTs had a very large surface area with high stability. Ru was employed to enhance the methanol oxidation activity of Pt catalyst. The use of Ru effectively promoted the activation of water and facilitated the concomitant transfer of oxygen to CO to produce CO₂. The 60:40 PtRu nanoparticles deposited on the TiO₂NTs had the highest surface area and activity of methanol oxidations when compared with other TiO₂NT/Pt and TiO₂NT/PtRu electrodes.

6.3 Oxygen reduction reaction on the TiO₂NT/rGO-PtRu electrodes

The oxygen reduction reaction at the cathode was studied in Chapter 5. Electrochemical deposition was employed to successfully synthesize the TiO₂NT/rGO-PtRu nanocomposite. SEM images and EDX mapping revealed that the rGO-PtRu nanomaterials with the Pt:Ru ratio of 64:36 were uniformly deposited onto the TiO₂NTs. The TiO₂NT/rGO-PtRu (64:36) electrode provided the best ORR enhancement. This unique performance was attributed to the behaviour of the PtRu nanoparticles and the strong interactions between rGO and TiO₂NT, which improved charge transport through the rGO. The TiO₂NT/rGO-PtRu electrode exhibited reduced charge transfer resistance and a much higher ORR activity. The high-performance of the TiO₂NT/rGO-PtRu nanocomposite suggests that it is promising for the enhancement of ORR and fuel cell applications.

6.4 Closing remarks and future work

The detrimental effects of environmental pollution are clear and promote the quest for alternate power generation sources that provide clean energy. The development of anodic catalysts for methanol oxidation and cathodic catalysts for oxygen reduction was the primary objective of this thesis. It was found that PtIr based nanomaterials are promising for methanol oxidation applications, which could be potentially incorporated into small vehicles and portable electronics. Certain atomic compositions of Pt with other metals, such as Ru and Ir are critical for anode material enhancement. The inclusion of Ru and Ir altered the number of available active sites on the TiO₂NT/Pt electrode, providing enhanced stabilization. Future work should focus on: (i) optimization of the experimental conditions for the growth of TiO₂ nanotubes; (ii) optimization of PtIr and PtRu based alloy geometries, composition and structure to further promote their catalytic activity and stability; (ii) investigation of the rGO-PtRu nanocomposites towards methanol oxidation; (iii) study of the rGO-PtIr nanocomposites for both methanol oxidation and oxygen reduction; and (iv) understanding of the mechanisms of the enhancement of the methanol oxidation as well as the oxygen reduction.